PB84-238260

Indirect Estimation of Convective Boundary Layer Structure for Use in Routine Dispersion Models

(U.S.) National Oceanic and Atmospheric Administration, Boulder, CO

Prepared for

Environmental Sciences Research Lab.
Research Triangle Park, NC

Aug 84

U.S. Department of Commerce
National Technical Information Service
NTIS

PB84-238260

EPA-600/3-84-091
August 1984

AN INDIRECT ESTIMATION OF CONVECTIVE BOUNDARY LAYER STRUCTURE FOR USE IN ROUTINE DISPERSION MODELS

by

James M. Wilczak
Cooperative Institute for Research in Environmental Sciences (CIRES)
University of Colorado/NOAA
Boulder, Colorado 80309

and

Mary Sue Phillips
National Oceanic and Atmospheric Administration/Environmental Research Laboratories
Boulder, Colorado 80303

Interagency Agreement AD-13-F2A059

Peter L. Finkelstein, Project Officer
Meteorology and Assessment Division

ENVIRONMENTAL SCIENCES RESEARCH LABORATORY
OFFICE OF RESEARCH AND DEVELOPMENT
U. S. ENVIRONMENTAL PROTECTION AGENCY
RESEARCH TRIANGLE PARK, NORTH CAROLINA 27711

REPRODUCED BY
NATIONAL TECHNICAL
INFORMATION SERVICE
U.S. DEPARTMENT OF COMMERCE
SPRINGFIELD, VA. 22161

TECHNICAL REPORT DATA
(Please read Instructions on the reverse before completing)

1. REPORT NO.	2.	3. RECIPIENT'S ACCESSION NO.
EPA-600/3-84-091		PB84 238260

4. TITLE AND SUBTITLE	5. REPORT DATE
AN INDIRECT ESTIMATION OF CONVECTIVE BOUNDARY LAYER STRUCTURE FOR USE IN ROUTINE DISPERSION MODELS	August 1984
	6. PERFORMING ORGANIZATION CODE
7. AUTHOR(S)	8. PERFORMING ORGANIZATION REPORT NO.
James M. Wilczak and Mary Sue Phillips	
9. PERFORMING ORGANIZATION NAME AND ADDRESS	10. PROGRAM ELEMENT NO.
National Oceanic and Atmospheric Administration ERL Wave Propagation Laboratory Boulder, Colorado 80303	CDTA1D/08-2189 (FY-84)
	11. CONTRACT/GRANT NO.
	AD-13-F2A059 (IAG)
12. SPONSORING AGENCY NAME AND ADDRESS	13. TYPE OF REPORT AND PERIOD COVERED
Environmental Sciences Research Laboratory--RTP,NC Office of Research and Development U. S. Environmental Protection Agency Research Triangle Park, NC 27711	Final
	14. SPONSORING AGENCY CODE
	EPA/600/09

15. SUPPLEMENTARY NOTES

16. ABSTRACT

Dispersion models of the convectively driven atmospheric boundary layer (ABL) often require as input meteorological parameters that are not routinely measured. These parameters usually include (but are not limited to) the surface heat and momentum fluxes, the height of the capping inversion Z_i, the mean windspeed, wind direction and temperature profiles up to Z_i, and the profiles of the turbulent wind components. Through use of a simple inversion rise model, surface layer flux-profile relationships, and similarity scaling laws for the convective ABL, we demonstrate how the required meteorological parameters can be deduced using much simpler and more readily available measurements. These measurements consist of an early morning temperature profile obtained from a radiosonde ascent; single level surface layer values of U, AZ, σ_u and σ_v; two levels of mean temperature near the surface; and an estimate of the local surface roughness.

Predicted values of each of the required parameters are compared to directly measured values of 26 days of data. Except for wind direction, each of these parameters can be estimated with an average error of 10-30%. For light windspeeds the mean wind direction profile is strongly affected by slight terrain inhomogenieties, and simple wind direction parameterizations fail. Finally, the role of averaging time in estimating the error of an individual realization is discussed.

17. KEY WORDS AND DOCUMENT ANALYSIS

a. DESCRIPTORS	b. IDENTIFIERS/OPEN ENDED TERMS	c. COSATI Field/Group

18. DISTRIBUTION STATEMENT	19. SECURITY CLASS *(This Report)*	21. NO. OF PAGES
RELEASE TO PUBLIC	UNCLASSIFIED	89
	20. SECURITY CLASS *(This page)*	22. PRICE
	UNCLASSIFIED	

EPA Form 2220-1 (Rev. 4-77) PREVIOUS EDITION IS OBSOLETE

NOTICE

This document has been reviewed in accordance with U. S. Environmental Protection Agency policy and approved for publication. Mention of trade names or commercial products does not constitute endorsement or recommendation for use.

ABSTRACT

Dispersion models of the convectively driven atmospheric boundary layer (ABL) often require as input meteorological parameters that are not routinely measured. These parameters usually include (but are not limited to) the surface heat and momentum fluxes $\overline{w'\theta'}$ and $\overline{u'w'}$, the height of the capping inversion Z_i, the mean windspeed $\overline{U}(z)$, wind direction $\overline{AZ}(z)$ and temperature profiles $\overline{\theta}(z)$ up to Z_i, and the profiles of the turbulent wind components $\sigma_u(z)$, $\sigma_v(z)$, and $\sigma_w(z)$. Through use of a simple inversion rise model, surface layer flux-profile relationships, and similarity scaling laws for the convective ABL, we demonstrate how the required meteorological parameters can be deduced using much simpler and more readily available measurements. These measurements consist of an early morning temperature profile obtained from a radiosonde ascent; single level surface layer values of $\overline{U}$, $\overline{AZ}$, σ_u and σ_v; two levels of mean temperature near the surface; and an estimate of the local surface roughness.

Predicted values of each of the required parameters are compared to directly measured values for 26 days of data. Except for $\overline{AZ}(z)$, each of these parameters can be estimated with an average error of 10-30%. For light windspeeds the mean wind direction profile is strongly affected by slight terrain inhomogenieties, and simple $\overline{AZ}(z)$ parameterizations fail. Finally, the role of averaging time in estimating the error of an individual realization is discussed.

CONTENTS

ABSTRACT..... iii

FIGURES..... vi

ACKNOWLEDGMENT..... viii

1. INTRODUCTION..... 1
   A) Purpose of the Analysis..... 2
   B) Procedures to be Used..... 3
   C) Instrumentation..... 3
   D) Experimental Conditions..... 3

2. SURFACE-LAYER ANALYSIS..... 6
   A) Flux-Profile Equations..... 6
   B) Surface Roughness Estimation..... 7

3. INVERSION RISE ANALYSIS..... 10
   A) Numerical Solution..... 10
      1) Initial conditions..... 12
      2) Numerical instabilities..... 15
   B) Analytic Solution..... 18

4. SELECTION OF DATA..... 23
   A) Data Quality..... 23
   B) Inversion Height Measurements..... 24

5. ABL PARAMETERIZATIONS..... 28
   A) Windspeed Profile..... 28
   B) Temperature Profile..... 28
   C) Wind Direction Profile..... 29
   D) Turbulent Velocity Profiles..... 29

6. RESULTS..... 32
   A) Surface Layer Predictions..... 32
   B) Mean ABL Predictions..... 42
   C) ABL Profiles..... 54

7. SUMMARY AND CONCLUSIONS..... 76

REFERENCES..... 79

FIGURES

Number		Page
1	Schematic of instrumentation systems used.....	4
2	Topographical map of the BAO area.....	9
3a-c	Morning temperature profiles and equivalent mixed-layer profiles.....	13
4	Z_i growing due to encroachment.....	17
5	Z_i growing due to entrainment starting from $\Delta\theta = 0$.....	17
6a-d	Schematic of roots of the equation $f(x) = x^7 = cx^5 - b$.....	21
7	Z_i determined from a tower or radiosonde temperature profile...	25
8	Z_i determined from the sodar return.....	26
9	Z_i determined from the lidar return.....	27
10a,b	Turbulent velocity profiles taken from laboratory tank experiments.....	30
11a,b	Turbulent velocity profiles taken from atmospheric measurements.....	30
12	Ensemble heat flux derived from the Kansas flux-profile relations.....	33
13a	Ensemble heat flux derived from the ITCE flux-profile relation vs. time.....	34
13b	Calculated vs. measured heat fluxes.....	35
13c	Ensemble heat flux bias and error vs. time.....	36
14a	As in 13a except for momentum flux.....	38
14b	As in 13b except for momentum flux.....	39
14c	As in 13c except for momentum flux.....	40
15a,b	Calculated vs. measured heat and momentum fluxes using 1 hour averages.....43,44	
16a,b	Z_i predictions and measured values as a function of time for 820916 and 830902.....46,47	
17a	Inversion heights, calculated vs. measured.....	48
17b	Ensemble calculated and measured inversion heights vs. time....	49

17c	Ensemble Z_i bias and error vs. time	50
18a	Inversion rise model calculated values of mean mixed layer temperature vs. measured values	52
18b	Ensemble calculated and measured mixed layer temperatures vs. time	53
19a	Profile derived temperature at the 150 m level vs. measured value	55
19b	Normalized mixed layer profiles of potential temperature	56
20a	Profile derived mean mixed layer temperature vs. measured value	58
20b	Ensemble profile derived and measured mixed layer temperature vs. time	59
21a	Calculated and predicted non-dimensional windspeed at 150 m	60
21b	Calculated and measured profiles of windspeed	61
22a	Wind direction profile relative to $\overline{AZ}_s$	63
22b	Bias and error of $\overline{AZ}(z)$ prediction	64
23a	Calculated and predicted non-dimensional longitudinal wind velocity profile	66
23b	Non-dimensional lateral wind velocity profile	67
24	Normalized profile of σ_w calculated and measured, using measured values of Z_i and $\overline{w'\theta'}_o$	68
25a	Calculated vs. measured values of σ_w at 150 m using calculated values of Z_i and $\overline{w'\theta'}_o$	69
25b	Non-dimensional calculated and measured values of σ_w using calculated values of Z_i and $\overline{w'\theta'}_o$	70
26a	As in 25a except for σ_u	72
26b	As in 25b except for σ_u	73
27a	As in 25a except for σ_v	74
27b	As in 25b except for σ_v	75

ACKNOWLEDGMENT

We would like to thank Bruce Turner, John Irwin, William Petersen, J. Chandran Kaimal and John Gaynor for their constructive comments and discussions.

SECTION 1

INTRODUCTION

The quality of any dispersion model which has been designed to predict the transport and diffusion of atmospheric pollutants will depend not only on the physical soundness of its parameterization of the diffusion process, but also on the quality of the meteorological data used as input to the model. In an ideal situation, a dispersion modeler would like to have the appropriate meteorological information directly measured as a function of the three spatial directions (x,y,z) and of time (t), or in the case of a horizontally homogeneous atmosphere, as a function of (z,t). Except in unusual situations where sophisticated in-situ or remote sensors are present, such information is not available. Instead, relatively simple measurements are made at few points in space and time, and these measurements are then extrapolated not only to other locations and times, but are also used to predict some meteorological parameters that are not measured at all.

The accuracy of this extrapolation process depends on our understanding of the physical processes which relate one atmospheric variable to another. During the past several decades considerable progress has been made in describing the mean and turbulent meteorological fields through semi-empirical theories. (These theories are generally based on the concept of "similarity", i.e., that when properly non-dimensionalized, the various meteorological

variables collapse onto single or similar curves.) In addition, theories based on penetrative convection have proven capable of predicting the growth of the mixed layer due to surface heating. At present, however, there exists a lag between these advances and the actual techniques used in the extrapolation of meteorological data for most dispersion models. The purpose of this analysis, therefore, is to draw together the various semi-empirical theories and to demonstrate that with only relative simple, routinely measured parameters, one can accurately deduce the mean and turbulent structure of the convective planetary boundary layer.

In this analysis we assume that the meteorological parameters required for dispersion calculations are the vertical profiles of $\overline{U}$, $\overline{AZ}$, $\overline{\theta}$, σ_u, σ_v, and σ_w up to the height of the capping inversion Z_i, as well as the surface heat flux $\overline{w'\theta'}$, and momentum flux, $\overline{u'w'}$. These parameters will need to be known as a function of time, beginning shortly after sunrise and continuing through the day until late afternoon. The direct measurements which will be used to predict these parameters consist of

1) an early morning temperature sounding, obtained from a rawinsonde ascent;

2) the mean surface wind speed $\overline{U}_s$ and direction $\overline{AZ}_s$ measured at one height (nominally 10 m) as well as the turbulent velocities σ_u and σ_v at the same height;

3) two levels of mean temperature near the surface, $\overline{\theta}_1$, and $\overline{\theta}_2$ (nominally 2 and 10 m);

4) an estimate of the local surface roughness, z_o.

The approach which we will take will be to estimate $\overline{w'\theta'}$ and $\overline{u'w'}$ by applying the surface layer flux-profile equations to $\overline{U}_s$, $\overline{\theta}_1$, $\overline{\theta}_2$ and z_o. The surface heat flux, stress and the morning temperature sounding will then be used to calculate the growth of Z_i during the day. Next, $\overline{w'\theta'}$, $\overline{u'w'}$, $\overline{\theta}$ and Z_i will be used to form the similarity scaling parameters L, u_*, and w_*. This then allows us to compute each of the required profiles from previously published mixed layer and surface layer similarity profiles.

Twenty six days of data are used in this analysis, which were taken in the late summer over two consecutive years at the Boulder Atmospheric Observatory as part of a larger EPA sponsored study of turbulent diffusion. The surface wind speed and direction, and heat flux and stress were measured with a 3-axis sonic anemometer-platinum wire thermometer system mounted on a short mast at a height of 9.8 m, located either 20 or 100 m west of the BAO tower. Also on the short mast were two aspirated quartz-crystal thermometers, mounted at either 2 and 8 m or 1.7 and 9.2 m, which measure the mean temperature with an accuracy of 0.05°C. In addition, the 300 m BAO tower has 8 levels of sonic anemometers and quartz-crystal thermometers, which provide direct measurements of the mean profiles and turbulent velocity moments for comparison to the indirect predictions. Finally, direct measurements of Z_i are obtained from the BAO tower, sodar, lidar and rawinsondes. Each of these instruments is indicated in Fig. 1.

The typical late summer meteorological diurnal cycle at the BAO site is as follows. During the night shallow drainage winds flow down from the foothills of the Front Range of the Rocky Mountains, and are channeled in an east-north-

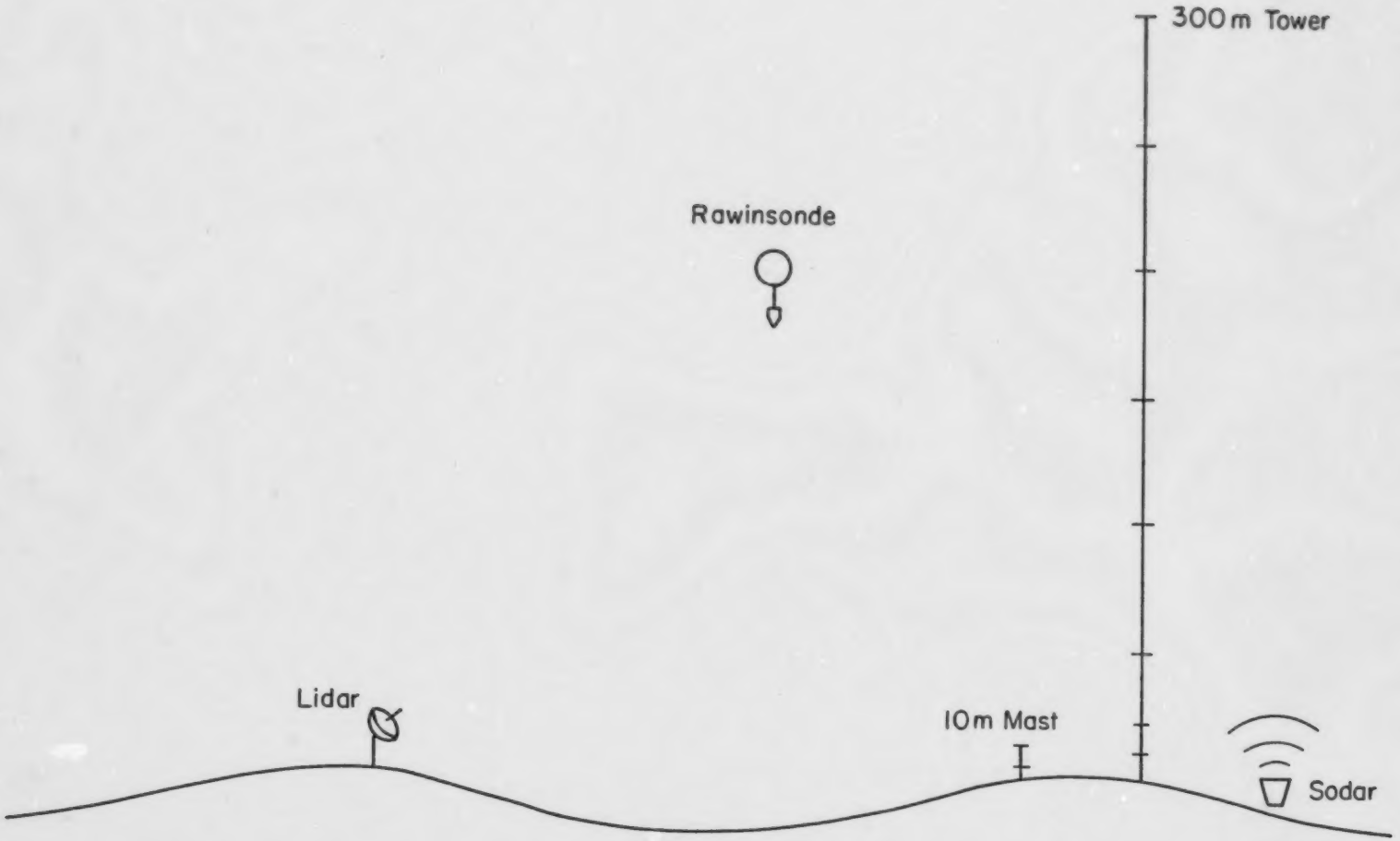

Fig. 1. Schematic of the instrumentation systems used.

easterly direction following the local terrain leading into the Platte River basin. After sunrise, surface heating begins to force an upslope component of the wind. By late morning this component usually becomes strong enough so that surface winds are from the east. Since the upper atmospheric flow typically has a westerly component, the PBL winds at the BAO are generally highly sheared. Experience shows that the easterly upslope component dominates in the lowest half of the PBL, gradually shifting to more westerly winds at Z_i. The upslope/downslope winds are of course superimposed on the synoptically forced flow, and may therefore at times be indiscernable. Moreover, mesoscale eddies often develop in the lee of the Front Range. These eddies, which have a diameter of ≈ 100 km, can rotate either cyclonically or anti-cyclonically depending on the synoptic forcing. Because of these eddies, upper level PBL winds at the BAO can show little relation to either the local synoptic surface pressure gradient or to upslope/downslope forcing.

Because terrain nonuniformity at the BAO site can result in a variety of dynamically or thermally forced mesoscale circulations, one would not expect simple parameterizations that were developed for simple, homogeneous boundary layers to work nearly as well. One might then consider this analysis to represent a reasonable "worst case" for the indirect estimation of the meteorological dispersion parameters.

SECTION 2

SURFACE LAYER ANALYSIS

The use of the surface layer flux-profile equations to estimate the fluxes of heat and momentum from measurements of mean wind speed and temperature is a well-known technique (Nieuwstadt, 1978). The flux-profile equations can be written as

$$\bar{U}(z,z_o,u_*,\theta_*) = \frac{u_*}{k}\{\ell n(z/z_o) - \psi_1(z/L)\} \tag{1}$$

$$\bar{\theta}(z,z_o,u_*,\theta_*) - \bar{\theta}_o = \frac{K_m}{K_h}\frac{\theta_*}{k}\{\ell n(z/z_o) - \psi_2(z/L)\} . \tag{2}$$

For unstable conditions

$$\psi_1 = 2\ell n(\frac{1+x}{2}) + \ell n(\frac{1+x^2}{2}) - 2\tan^{-1}(x) + \pi/2 \tag{3}$$

$$\psi_2 = 2\ell n(\frac{1+y}{2}) \tag{4}$$

where $$x = (1 - \gamma_1\, z/L)^{1/4} \tag{5}$$

$$y = (1 - \gamma_2\, z/L)^{1/2} . \tag{6}$$

Here $\theta_* = -\overline{w'\theta'_o}/u_*$, $L = -u_*^3/(k\, g/\bar{\theta}\, \overline{w'\theta'_o})$, while k, K_m/K_h, γ_1 and γ_2 are empirically determined constants.

Rewriting (1) and (2) as

$$u_* = \frac{k\bar{U}(z_1)}{\ell n(z_1/z_o) - \psi_1(z_1/L)} \tag{7}$$

$$\theta_* = \frac{k(\bar{\theta}(z_3) - \bar{\theta}(z_2))}{(K_m/K_h)[\ln(z_3/z_1) - \psi_2(z_3/L) + \psi_2(z_2/L)]} \tag{8}$$

we solve for u_* and θ_* using the following iterative procedure:

1) Assume $L = -\infty$; $\psi_1 = \psi_2 = 0$
2) Solve for u_* and θ_*
3) Calculate a new L, ψ_1 and ψ_2
4) Test if $|1 - \frac{L_{old}}{L_{new}}| < \varepsilon$

   where ε is a small number (0.0005). If the convergence test is met, stop; if not return to step 2.

The accuracy of this method depends not only on the validity of the flux-profile formulations, but also on the assumed value of the surface roughness, z_o. Visual estimates of z_o at the BAO site, based on the local ground cover (plowed fields, wheat stubble, tall grass) are $z_o \approx$ 1-2 cm. A study by Oncley and Kahn (personal communication) of the wind profiles near the BAO in April using a 4 m mast do in fact provide a z_o of ~1 cm. In contrast the analysis of Schotz and Panofsky (1980) and Korrell et al. (1982) using wind measurements from the lowest 100 m of the BAO suggest that $z_o \approx$ 6-30 cm, with the higher roughnesses found for winds from the southeast. This discrepancy suggests that the wind profiles may depart from (1) and (2) so that an effective z_o increases with height. This is a reasonable assumption if the lower level wind profile is in equilibrium with the nearby roughness elements (ground cover) while the upper level wind profile is in equilibrium with roughness elements averaged over a greater horizontal area including trees, fences, houses, and rolling hills (Fig. 2).

Because of the uncertainty in the surface roughness and of its variability with height, we estimated z_o using only 10 m level data, since this level

would most closely correspond to the height of the available measured values $\overline{U}(z_1)$, $\overline{\theta}(z_2)$ and $\overline{\theta}(z_3)$. This was done by rewriting (1) as

$$z_o = z_1 \exp\left[-\frac{k\overline{U}(z_1)}{u_*} + \psi_1(z_1/L)\right] \tag{9}$$

where u_* and L are both measured at a height of $z_1 \approx 10$ m. Because z_o varies with the exponential of the term in brackets, this method introduces a large amount of scatter into the z_o estimates. If however, the mean profiles adjust with height to a varying $z_o(z)$, it is desirable to use such a method because it gives z_o at the particular height in question.

Thirty eight hours of data taken during convectively unstable to near neutral conditions were analyzed using (9). The data came from two years of measurements taken during August and September at the BAO. Only periods with $\overline{U} > 5$ ms^{-1} were used. The function ψ_1 was calculated using two different flux-profile relations. The first were the Kansas flux-profiles (Businger et al., 1971): $k = 0.35$, $K_m/K_h = 0.74$, $\gamma_1 = 15$ and $\gamma_2 = 9$. The second set of constants were those reported for the ITCE experiment by Dyer and Bradley (1982): $k = 0.40$, $K_m/K_h = 1.0$, $\gamma_1 = 28$ and $\gamma_2 = 15$. The Kansas profiles gave $z_o = 5.85 \pm 3.61$ cm, while the ITCE profiles gave $z_o = 2.79 \pm 1.76$ cm. The indirect estimation of the surface heat flux and stress was then carried out using both sets of profiles, each using the appropriate z_o value determined above.

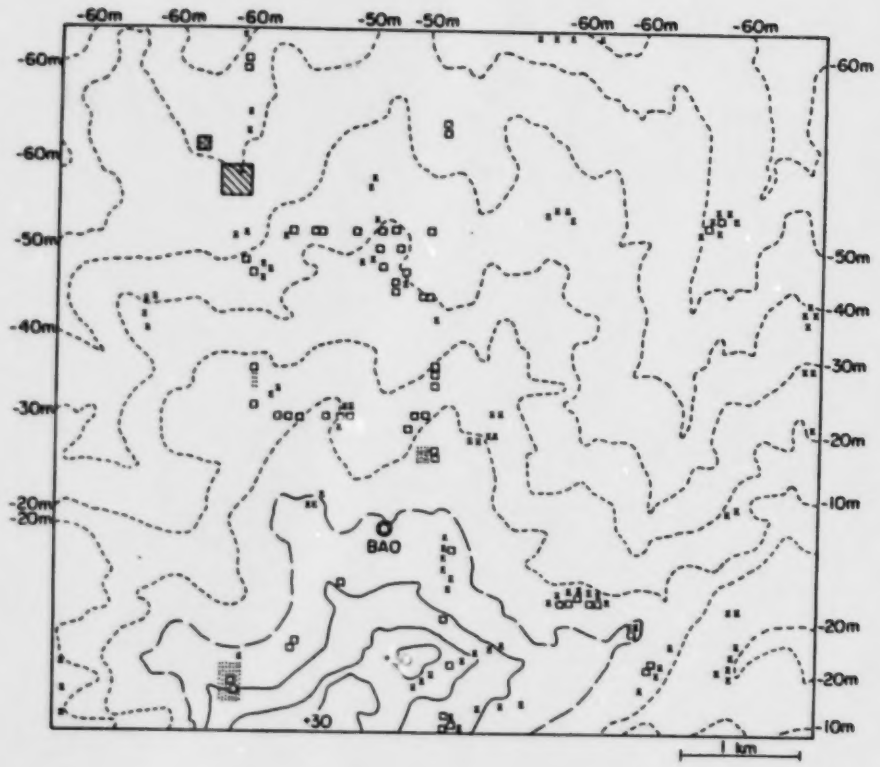

Fig. 2. Topographic map of the BAO area, with X's representing trees, □'s buildings, and stippling representing areas containing many smaller obstructions.

SECTION 3

INVERSION RISE ANALYSIS

For the conditions of a negligible synoptic scale mean vertical velocity, the equations which govern the rate of growth of the convectively driven mixed layer are given by

$$\frac{d\theta_{BL}}{dt} = \frac{1}{Z_i}\left(\overline{w'\theta'}_o - \overline{w'\theta'}_i\right) \tag{10}$$

$$\frac{d\Delta\theta}{dt} = \gamma\frac{dZ_i}{dt} - \frac{d\theta_{BL}}{dt} = -\frac{\overline{\gamma w'\theta'}_i}{\Delta\theta} - \frac{\left(\overline{w'\theta'}_o - \overline{w'\theta'}_i\right)}{Z_i} \tag{11}$$

$$\frac{dZ_i}{dt} = -\frac{\overline{w'\theta'}_i}{\Delta\theta} \tag{12}$$

$$-\overline{w'\theta'}_i = A\,\overline{w'\theta'}_o + B\,u_*^3\,\overline{\theta}/gZ_i\ . \tag{13}$$

Here θ_{BL} is the mixed layer temperature, Z_i is the mixed layer depth, $\overline{w'\theta'}_o$ and $\overline{w'\theta'}_i$ are the surface and inversion level heat fluxes, $\Delta\theta$ is the temperature jump at the inversion ($\Delta\theta > 0$), and γ is the lapse rate above the inversion. Equation (13) represents a closure assumption based on laboratory and atmospheric measurements with A = 0.2 and B = 5. This set of equations is discussed by Tennekes (1973) and in more detail by Driendonks (1982a,b).

Since (10-13) are a non-linear set of differential equations, their solution must be found by numerical integration. To proceed with the integration we rewrite (11) and (12) as

$$\frac{dy1}{dt} = \frac{\gamma a_1(t)}{y1} - \frac{a_2(t)}{y2} = f_1(t,y1,y2) \tag{14}$$

$$\frac{dy2}{dt} = \frac{a_1(t)}{y1} = f_2(t,y1) \tag{15}$$

where $y1 = \Delta\theta$, $y2 = Z_i$ and

$$a_1(t) = (A\ \overline{w'\theta'}_o + B\ u_*^3\ \overline{\theta}/gZ_i) \tag{16}$$

$$a_2(t) = (1+A)\ \overline{w'\theta'}_o + B\ u_*^3\ \overline{\theta}/gZ_i\ . \tag{17}$$

Since we have two coupled equations (for y1 and y2) we need to integrate both simultaneously. To do so we use the following fourth-order Runge-Kutta scheme.

$$y1_{n+1} = y1_n + 1/6(m_{a1} + 2m_{b1} + 2m_{c1} + m_{d1}) \tag{18}$$

$$y2_{n+1} = y2_n + 1/6\ (m_{a2} + 2m_{b2} + 2m_{c2} + m_{d2}) \tag{19}$$

where $m_{a1} = \delta f_1(t_n,\ y1_n,\ y2_n)$ (20)

$$m_{a2} = \delta f_2(t_n,\ y1_n) \tag{21}$$

$$m_{b2} = \delta f_1(t_n + \delta/2,\ y1_n + m_{a1}/2,\ y2_n + m_{a2}/2) \tag{22}$$

$$m_{b2} = \delta f_2(t_n + \delta/2,\ y1_n + m_{a1}/2) \tag{23}$$

$$m_{c1} = \delta f_1(t_n + \delta/2,\ y1_n + m_{b1}/2,\ y2_n + m_{b2}/2) \tag{24}$$

$$m_{c2} = \delta f_2(t_n + \delta/2,\ y1_n + m_{b1}/2) \tag{25}$$

$$m_{d1} = \delta f_1(t_n + \delta,\ y1_n + m_{c1},\ y2_n + m_{c2}) \tag{26}$$

$$m_{d2} = \delta f_2(t_n + \delta,\ y1_n + m_{c1}) \tag{27}$$

and where δ is the time-step of the integration. Once $\Delta\theta$ and Z_i are computed at time t_{n+1}, $\theta_{BL}(t_{n+1})$ is found from (10).

To begin the integration initial values of $y1 = \Delta\theta_o$ and $y2 = Z_{i_o}$ and θ_{BL_o} are needed. If the early morning sounding is taken sufficiently long after sunrise so that a shallow mixed layer has developed, $\Delta\theta_o$, Z_{i_o} and θ_{BL_o} can be taken directly from the sounding. If however the morning sounding is taken before a mixed layer develops, an alternate method must be used. The scheme we use transforms the actual morning sounding $\overline{\theta}(z)$ profile into an equivalent mixed-layer profile which has the same net heat deficit (Driendonks, 1982a). This can be expressed as

$$\int_o^{Z_{i_o}} (\theta_o + \gamma z - \theta_{obs}(z)) = \int_o^{Z_{i_o}} (\theta_o + \gamma z - \theta_{model}(z))dz$$

$$= Z_{i_o} \Delta\theta_o - 1/2\ \gamma Z_{i_o}^2 , \tag{28}$$

where $\theta_o + \gamma z$ is a reference profile defined by extrapolating the upper level temperature profile to the surface (Figs. 3a-c).

For the case of a constant $\gamma(z)$ below Z_{i_c} (Fig. 3a), $\theta_o + \gamma z$ equals $\theta_{obs}(z)$, so (28) reduces to

$$\Delta\theta_o = 1/2\ \gamma Z_{i_o} = 1/2(\theta(Z_{i_o}) - \theta_o) \tag{29}$$

which then gives

$$\theta_{BL_o} = \theta_o + \Delta\theta_o . \tag{30}$$

Conservation of the net heat deficit provides a relationship between $\Delta\theta_o$ and Z_{i_o}, but it does not provide their values separately. One of the two

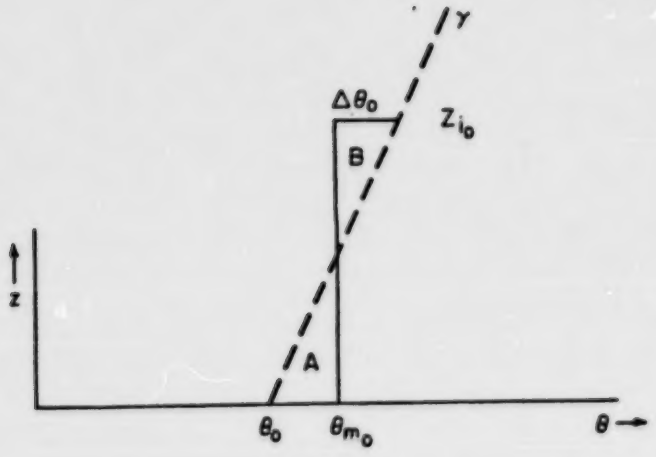

(a)

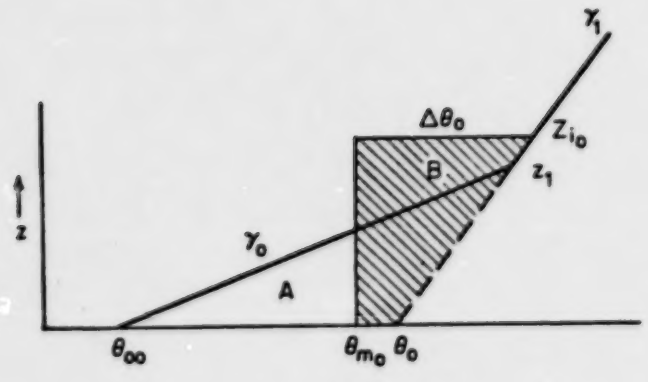

(b)

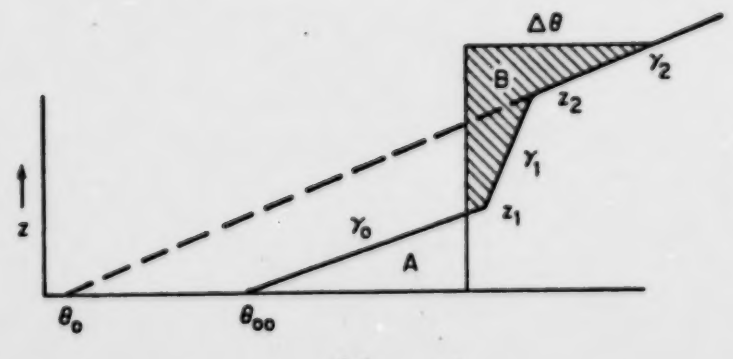

(c)

Fig. 3. Morning temperature profiles and equivalent mixed-layer profiles for a) constant γ, b) two levels of γ, and c) three levels of γ.

must be specified independently. Fortunately, the specific values of Z_{i_o} and $\Delta\theta_o$ are not important in determining the mixed layer character for times $t >> t_o$. Driedonks (1982b) has shown that for $Z_i = 3Z_{i_o}$, Z_{i_o}'s influence on determining the future growth of Z_i has decreased to 0.1% of its initial value. In other words, although it is important for the net heat deficit to be conserved, Z_i is soon determined principally by γ and $\overline{w'\theta'}_o$, and not by Z_{i_o}. Because of this we have considerable latitude in our choice of Z_{i_o}, especially if we are interested in times when $Z_i >> Z_{i_o}$. In our integration we used $Z_{i_o} = 50$ m, and then calculated $\Delta\theta_o$ to conserve the heat deficit. (As an aside, this height was typical of the depth of the nocturnal boundary layer at sunrise as determined by the BAO acoustic sounder).

In Fig. 3a we have assumed that the morning value of $\gamma(z)$ is constant up to Z_{i_o}, which is not always the case. For a one-level change of $\gamma(z)$ below Z_{i_o} (Fig. 3b), the conservation of the heat deficit gives

$$\Delta\theta_o Z_{i_o} = 1/2\ \gamma_1 Z_{i_o}^2 + (\theta_o - \theta_{oo})\ z_1 + 1/2(\gamma_1 - \gamma_o)\ z_1^2 \qquad (31)$$

while for a two-level change in $\gamma(z)$ below Z_{io} (Fig. 3c), we have

$$\Delta\theta_o Z_{i_o} = 1/2\ \gamma_2 Z_{i_o}^2 + (\theta_o - \theta_{oo})\ z_1 + 1/2(\gamma_2 - \gamma_o)\ z_1^2$$
$$+ (\theta_o - \theta_1 - \gamma_o z_1)(z_2 - z_1) + 1/2(\gamma_2 - \gamma_1)(z_2^2 - z_1^2). \qquad (32)$$

The number of rawinsonde levels reported below 50 m was never greater than 3, so (30-32) cover all possible cases encountered in the rawinsonde profiles.

Initially a time step of $\delta = 20$ min was used in the numerical integration. However, it was found that for small values of γ, $\Delta\theta$ would become small, and

this large of a time would lead to numerical instabilities. In these situations the increase in Z_i would be as much as a factor of 10 too large. Concomitant with the incorrectly large jump in Z_i would be a jump in $\Delta\theta$. The jump in $\Delta\theta$ would then act as a stabilizing factor, so that in the next time step Z_i would barely increase at all. In this sense the numerical integration is self-correcting. That is, the solution for Z_i cannot keep increasing incorrectly step after step in the integration process.

In all cases the numerical instability could be eliminated by using a smaller step in the integration process, as long as the lapse rate was positive. (For $\gamma \equiv 0$ the integration was always unstable.) The problem from an operational standpoint is to know how small of a time step is needed so that the numerical instability can be avoided.

The solution of this problem has two requirements. First, the value of $\gamma(z)$ must be positive. We chose a lower bound to be .0003, which corresponds to 0.3°C per kilometer. (Resolving a γ smaller than this seems to be outside the limits of the accuracy of the rawinsonde in any case.) Second, we test the calculated value of δZ_i at each step of the integration process (m_{a2}, m_{b2}, m_{c2} and m_{d2}) to check if it is smaller than a reasonable upper bound, δZ_{imax}. If $\delta Z_i > \delta Z_{imax}$, the integration step is repeated with a smaller time increment. This process continues with smaller time steps until $\delta Z_i < \delta Z_{imax}$. (The time steps used are 20, 10, 5, 2.5 and 1 minute.)

Since the instability problem occurs as $\Delta\theta \to 0$, we consider the limiting case of encroachment, that is $\Delta\theta \equiv 0$. In this case no energy goes into entrainment, but only into filling in the profile (Fig. 4). Over a time δt we can write

$$\text{input energy} = \overline{w'\theta'}\,\delta t$$

$$\text{encroachment energy} = Z_i(\theta_{i+1} - \theta_i) + 1/2(\theta_{i+1} - \theta_i)\,\delta Z_i \quad . \tag{33}$$

Also, since

$$\theta_{i+1} - \theta_i = \gamma \delta Z_i \tag{34}$$

we can write

$$\overline{w'\theta'}\,\delta t = Z_i\,\gamma\,\delta Z_i + 1/2\,\gamma(\delta Z_i)^2 \quad . \tag{35}$$

Solving for δZ_i we have

$$\delta Z_i = -Z_i + [Z_i^{\,2} + \frac{2}{\gamma}\,\overline{w'\theta'}\,\delta t]^{1/2} \tag{36}$$

The encroachment condition is a hypothetical limit which in fact never exists if $\gamma > 0$, because some entrainment will occur which makes $\Delta\theta$ non-zero. The energy that goes into entrainment (Fig. 5) will be given by

$$0.2\,\overline{w'\theta'}\,\delta t + \frac{5u_*^{\,3}\bar{\theta}}{g\,Z_i}\,\delta t = 1/2\,\Delta\theta\,\delta Z_i \quad . \tag{37}$$

But we can also write

$$\Delta\theta = \gamma\,\delta Zi \tag{38}$$

so that

$$\delta Z_i = [\frac{0.4\,\overline{w'\theta'}\,\delta t}{\gamma} + \frac{2\delta t}{\gamma}\,\frac{5u_*^{\,3}\bar{\theta}}{g\,Z_i}]^{1/2} \quad . \tag{39}$$

As an upper limit we combine both (36) and (39) to obtain

$$-Z_i + [Z_i^{\,2} + \frac{2}{\gamma}\,\overline{w'\theta'}_o\,\delta t]^{1/2} + [\frac{0.4\,\overline{w'\theta'}_o\,\delta t}{\gamma} + \frac{2\delta t}{\gamma}\,\frac{5u_*^{\,3}\bar{\theta}}{g\,Z_i}]^{1/2} \tag{40}$$

Finally, we note that (40) has been derived for $\Delta\theta = 0$. In fact $\Delta\theta$ is always positive, which further insures that (40) will never underpredict the maximum physically realistic change in Z_i.

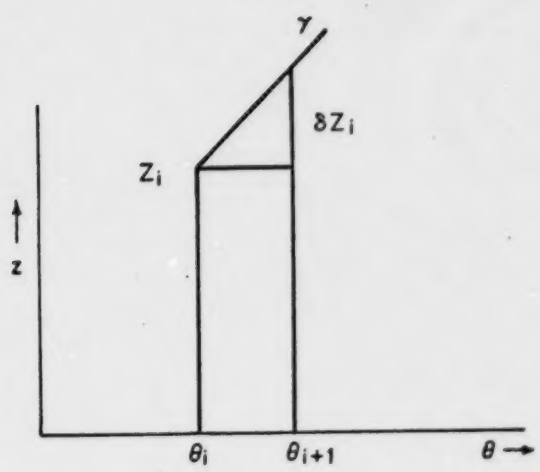

Fig. 4. Z_i growth due to encroachment.

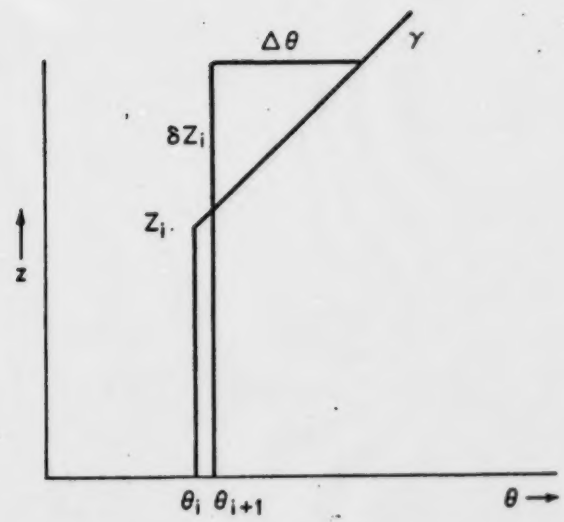

Fig. 5. Z_i growth due to entrainment starting from $\Delta\theta = 0$.

Driedonks (1982b) has shown that if the shear contribution in (13) is dropped, that the system of equations (10-13) is simplified such that an analytic solution can be found. This solution is given by

$$\frac{1}{2}\gamma\frac{A}{1+2A}Z_i^2 - \left(\frac{Z_{i_o}}{Z_i}\right)^{1/c}\left(Z_{i_o}\Delta\theta_o - \gamma\frac{A}{1+2A}Z_{i_o}^2\right) = A\left[I(t) + \frac{1}{2}\gamma Z_{i_o}^2 - Z_{i_o}\Delta\theta_o\right] \tag{41}$$

or
$$(Z_i/Z_{i_o})^2 - b(Z_i/Z_{i_o})^{-5} - c = 0 \tag{42}$$

where
$$b = \frac{\left(Z_{i_o}\Delta\theta_o - \gamma\frac{A}{1+2A}Z_{i_o}^2\right)}{\frac{1}{2}\gamma\frac{A}{1+2A}} \tag{43}$$

$$c = \frac{A\left[I(t) + \frac{1}{2}\gamma Z_{i_o}^2 - Z_{i_o}\Delta\theta_o\right]}{\frac{1}{2}\gamma\frac{A}{1+2A}Z_{i_o}^2} \tag{44}$$

and
$$I(t) = \int_o^t \overline{w'\theta'}(t')dt' \ . \tag{45}$$

The analytic solution provides us with a means of testing the full numerical solution by setting $u_* = 0$. To find the analytic solution we wish to find the roots of (42). This is done using Newton's method of successive approximations (Swokowski, 1979).

Although the application of Newton's method is straightforward, proving that the root that it has found is in fact the correct root is quite involved. We begin by rewriting (42) as

$$f(x) = x^7 - cx^5 - b = 0 \ . \tag{46}$$

and by noting that for A = 0.2

$$b < 0 \text{ if } Z_{i_o}\Delta\theta_o < 1/7\ \gamma Z_{i_o}^2$$

$$b > 0 \text{ if } Z_{i_o}\Delta\theta_o > 1/7\ \gamma Z_{i_o}^2$$

SECTION 6

RESULTS

Surface fluxes of heat and momentum were calculated using both the Businger-Dyer Kansas and ITCE forms of the flux-profile equations (see Section 2). The calculated fluxes were then compared to the fluxes measured at a height of 9.16 m on the small mast located west of the BAO tower. All periods when the wind blew through the sonic mast support ($310° < \overline{AZ} < 347°$) have been eliminated. Fluxes were computed for each 20 min period normally starting from approximately 40 min after sunrise. Ensemble values were then calculated by averaging together the same 20 min periods relative to sunrise, using only times when both measured and calculated values were available.

Ensemble heat flux values using the Kansas flux-profiles are shown in Fig. 12. Sunrise occurs at t = 0, while sunset approximately 12 hours later at t = 35. Curve A represents the measured flux, while B is the calculated flux. In the early morning and late afternoon periods the measured and calculated fluxes agree quite well, while the calculated flux underestimates the measured value by ≈ 25% during the middle part of the day.

ITCE profile derived heat fluxes are shown in Fig. 13a. The calculated flux is still underestimated during mid-day hours, but now by only ≈10%. Furthermore, the flux is slightly overestimated during the morning hours, so that the net daily averaged heat fluxes are in almost exact agreement.

$$c > 0 \text{ if } \int_o^t \overline{w\theta}\, dt' + 1/2\ \gamma\ Z_{i_o}{}^2 > Z_{i_o}\ \Delta\theta_o$$

$$c < 0 \text{ if } \int_o^t \overline{w\theta}\, dt' + 1/2\ \gamma\ Z_{i_o}{}^2 < Z_{i_o}\ \Delta\theta_o\ .$$

To plot f(x) we note that:

$$f(0) = -b$$

$$f(1) = 1 - b - c$$

$$\partial f/\partial x = 7x^6 - 5cx^4 \tag{47}$$

so that $x = 0$

$$x = \pm\ (\tfrac{5}{7}\ c)^{1/2}$$

are extrema if $c > 0$. If $c < 0$ there are no extrema. Also,

$$\partial^2 f/\partial x^2 = 42\ x^5 - 20\ cx^3 \tag{48}$$

is zero at $x = 0$, so that f(0) is an inflection point with zero slope. It can also easily be shown that (48) evaluated at $x = + \sqrt{(5/7)c}$ is positive, so that f(x) is concave upward at its positive extremum. Likewise at $x = - \sqrt{(5/7)c}$ (48) is negative.

From the above information we are able to qualitatively sketch f(x) for the four combinations of b and c positive or negative (Figs. 6a-d).

First we consider the case of no positive roots (Fig. 6a) when $c < 0$ and $b < 0$. This requires that

$$Z_{i_o}\ \Delta\theta_o < 1/7\ \gamma\ Z_{i_o}{}^2 \tag{49}$$

and $$I(t) + 1/2\ \gamma\ Z_{i_o}{}^2 < Z_{i_o}\ \Delta\theta_o\ . \tag{50}$$

But if (49) is true then

$$Z_{io}\,\Delta\theta_o < 1/2\,\gamma\,Z_{io}^{\,2} \tag{51}$$

and (50) cannot also be true, so that this case is not physically realizable. Further, if b = 0, then c > 0, with c = 0 only at time t = 0. In this case we will get one positive root for any time t > 0.

Next we consider the situation when there are two positive roots (Fig. 6c), i.e., when c > 0 and b < 0. The problem here is to ascertain which of these two roots is the correct one, and to determine if Newtons method will always find it.

First we note that the first positive zero occurs for

$$x = Z_i/Z_{i_o} < \sqrt{(5/7)c}\ . \tag{52}$$

Since $Z_i/Z_{i_o} > 1$, (52) implies that

$$\left[\frac{5/7\left\{I(t) + \frac{1}{2}\,\gamma\,Z_{i_o}^{\,2} - Z_{i_o}\,\Delta\theta_o\right\}(1+A)}{1/2\,\gamma Z_{i_o}^{\,2}}\right]^{1/2} > 1 \tag{53}$$

or

$$I(t) > Z_{i_o}\,\Delta\theta_o. \tag{54}$$

For very small times (54) will not be true, and the first root can be rejected on the basis that it requires $Z_i/Z_{i_o} < 1$. Since f(x) varies continuously with time, we will never get the first root to be the real solution, because to do so would require a sudden jump in Z_i from the second root to its first.

The problem now is to insure that Newton's method converges to the larger

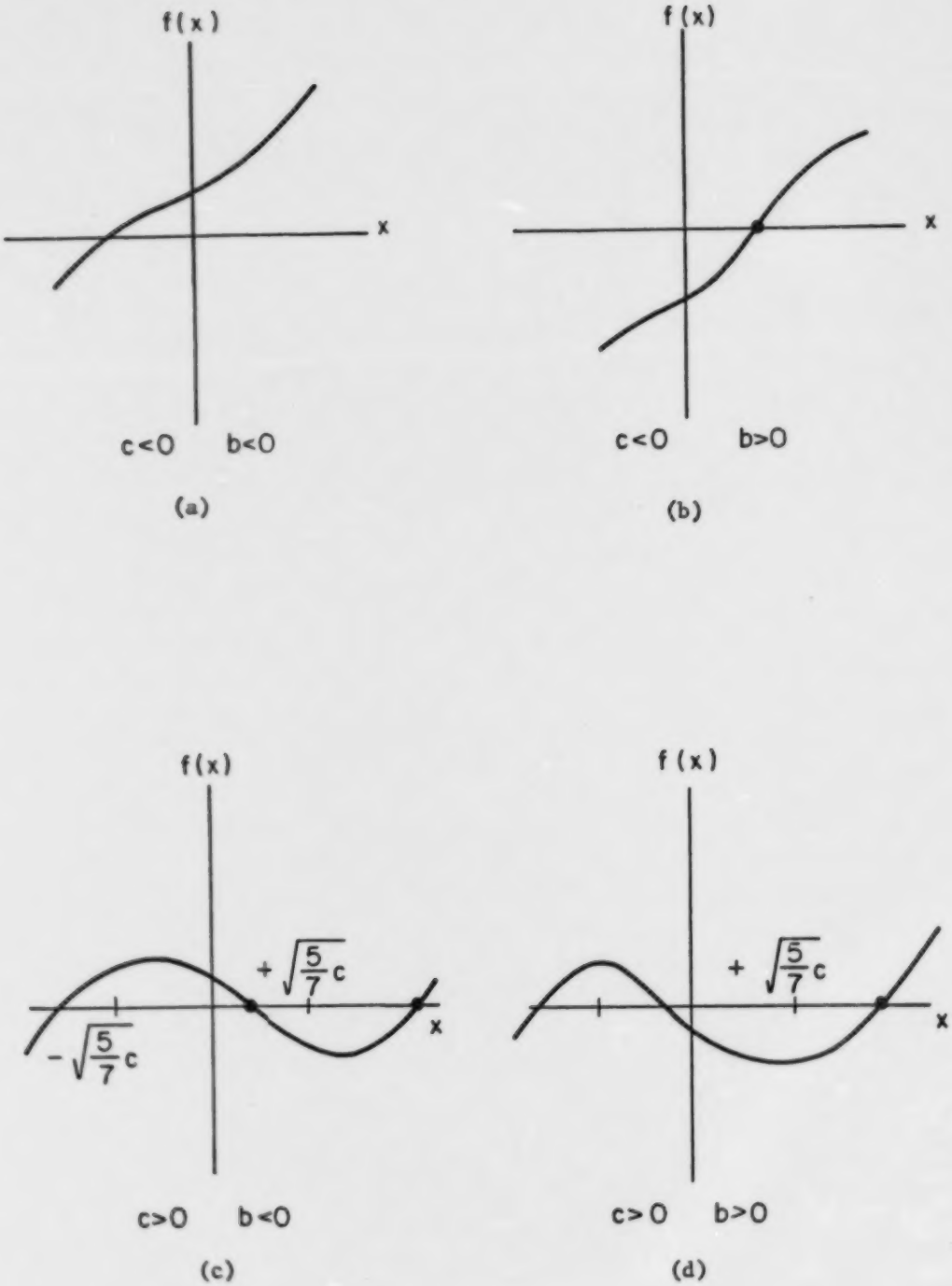

Fig. 6. Schematic of roots of the equation $f(x) = x^7 - cx^5 - b$ for four possible combinations of $b \gtrless 0$ and $c \gtrless 0$.

root. From the above discussion we can see that this will only be a problem for times sufficiently large such that $\sqrt{(5/7)c} > 1$. But at times with Z_i considerably larger than Z_{i_o} (42) reduces to

$$(Z_i/Z_{i_o})^2 = c \ . \tag{55}$$

Using $Z_i/Z_{i_o} = + \sqrt{c}$ as an initial guess for Newton's method then insures that the solution will converge to the larger (and correct) of the two roots.

The analytic solution has been used to insure that the computer code for the numerical solution is in fact working. For cases where u_* is small, the analytic solution can in fact be used in place of the numerical solution. However, since the analytic solution also requires a numerical approach (Newton's method) it is not of any great advantage, either in terms of computational time or simplicity.

SECTION 4

SELECTION OF DATA

Although the theories and similarity laws used in the estimation of the PBL structure are strictly intended only for quasi-stationary, horizontally homogeneous, barotropic boundary layers, no attempt was made to eliminate days when these conditions did not apply. This is because the indirect method is meant to be used in an operational mode, without regard to the actual PBL state. In fact, information on baroclinicity, horizontal homogeniety, or even stationarity is unlikely to be available on a routine basis. The question then reduces to asking how well the similarity scaling laws hold in all meteorological conditions. Although there was no intentional editing of the data for non-ideal conditions, there nevertheless was some "filtering" due to the fact that on cloudy, frontal-passage days no data was taken.

Data from the BAO is routinely averaged and archived over 20 min intervals. For this reason all of the computations were done using 20 min mean values, as were the comparisons between predicted and measured values. Both the BAO tower and 10 m tower data were edited for wind shadowing effects, due to the wind blowing through the tower support structure. The tower instrumentation was located on the SSE boom, so that northerly winds have been eliminated from the data set.

The early morning soundings used for the inversion rise model initialization were all taken within 1 hour of sunrise, with most being taken 10 to 15

minutes prior to sunrise. Each sounding was reduced by hand to give no more than 10 levels of $\gamma(z)$.

Direct measurements of Z_i were provided by the temperature profile from the 300 m BAO tower, from the BAO sodar (under ideal conditions good up to 680 m), from a NOAA lidar system (which has a virtually unlimited vertical range), and from the temperature profiles of rawinsonde ascents. Examples of each of these measurements and their respective Z_i values shown in Figs. 7-9.

Inversion height values were tabulated for 20 min periods, corresponding to the same times recorded by the BAO tower. Because the inversion rise model uses a 20 min average surface heat flux and stress, each value of the calculated Z_i corresponds to the end of that 20 min period. Measured values were therefore tabulated for a 20 min period centered at the <u>end</u> of each BAO tower period. The sodar values are simply 20 min averages of the backscatter returns. If more than one lidar measurement was available for each 20 min period they were averaged together. Tower measurements at time t_i and t_{i+1} were averaged to find an inversion height corresponding to the calculated value using $\overline{w'\theta'}$ and u_* from period t_i.

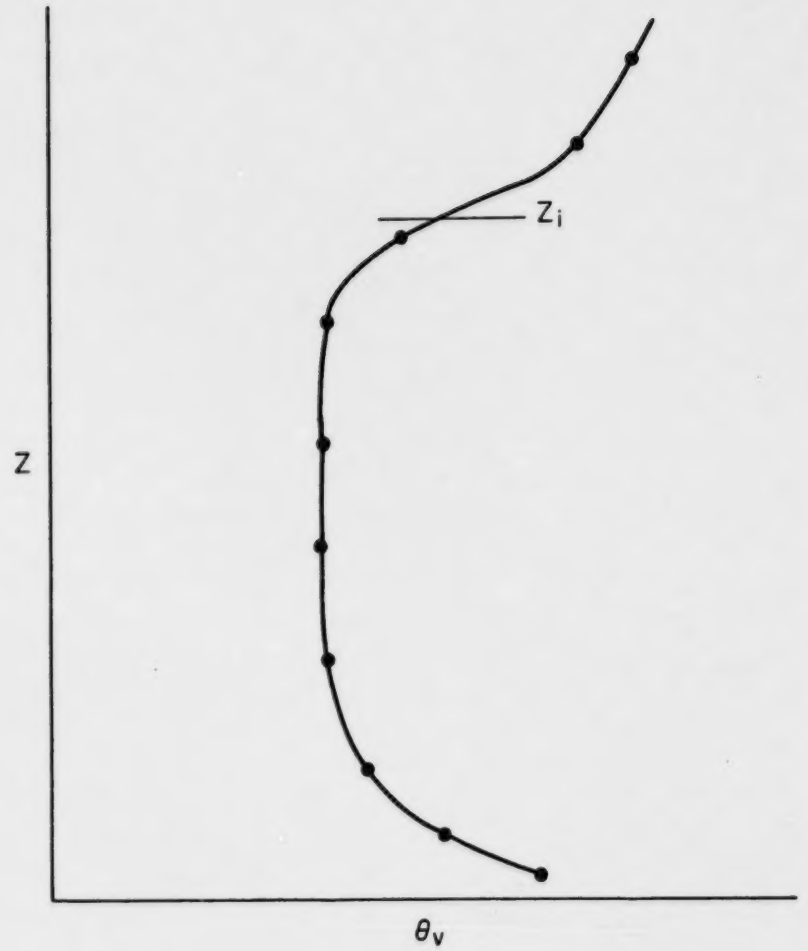

Fig. 7. Z_i determined from a tower or radiosonde temperature profile.

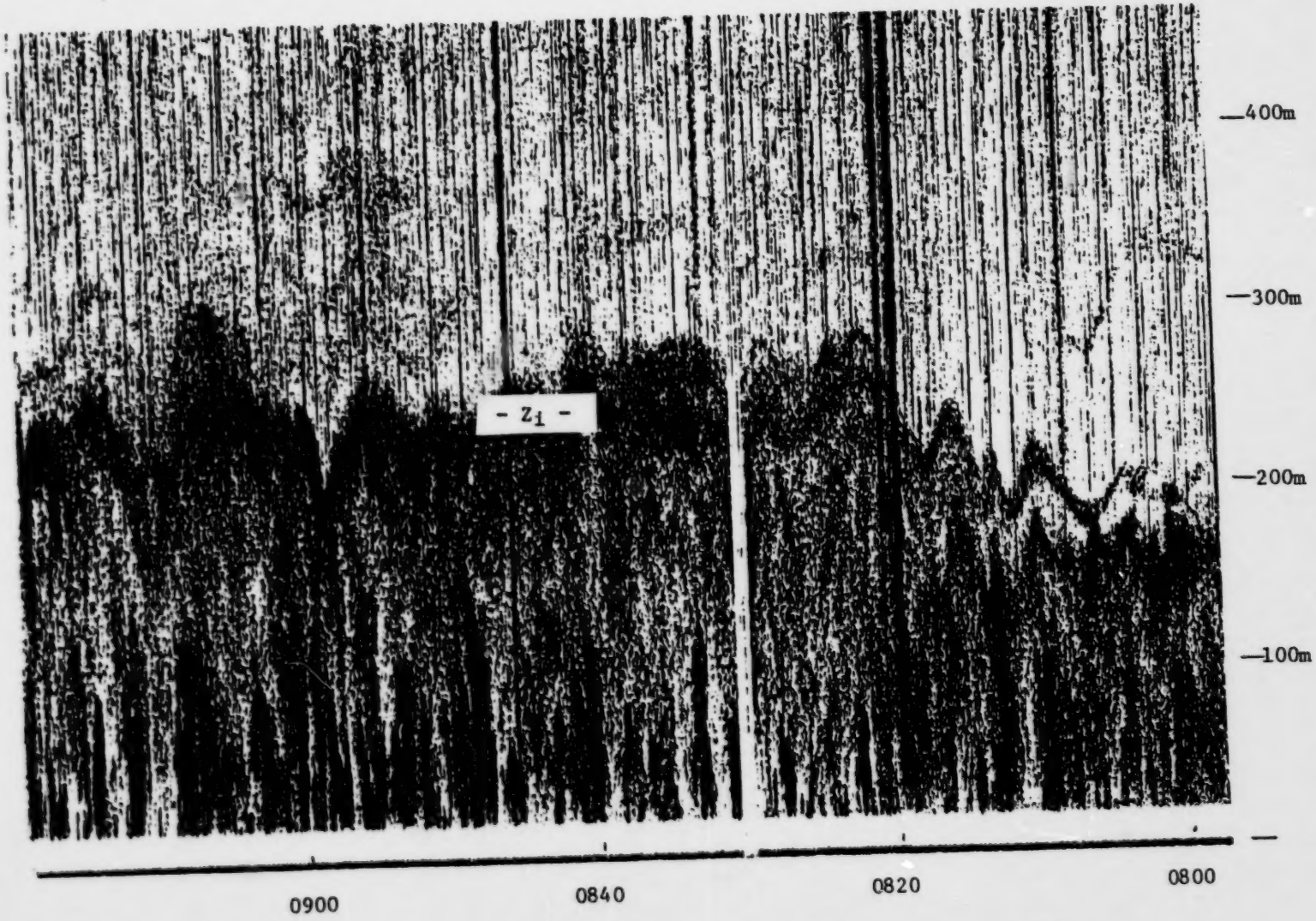

Fig. 8. Z_i determined from the sodar return on the morning of 830907.

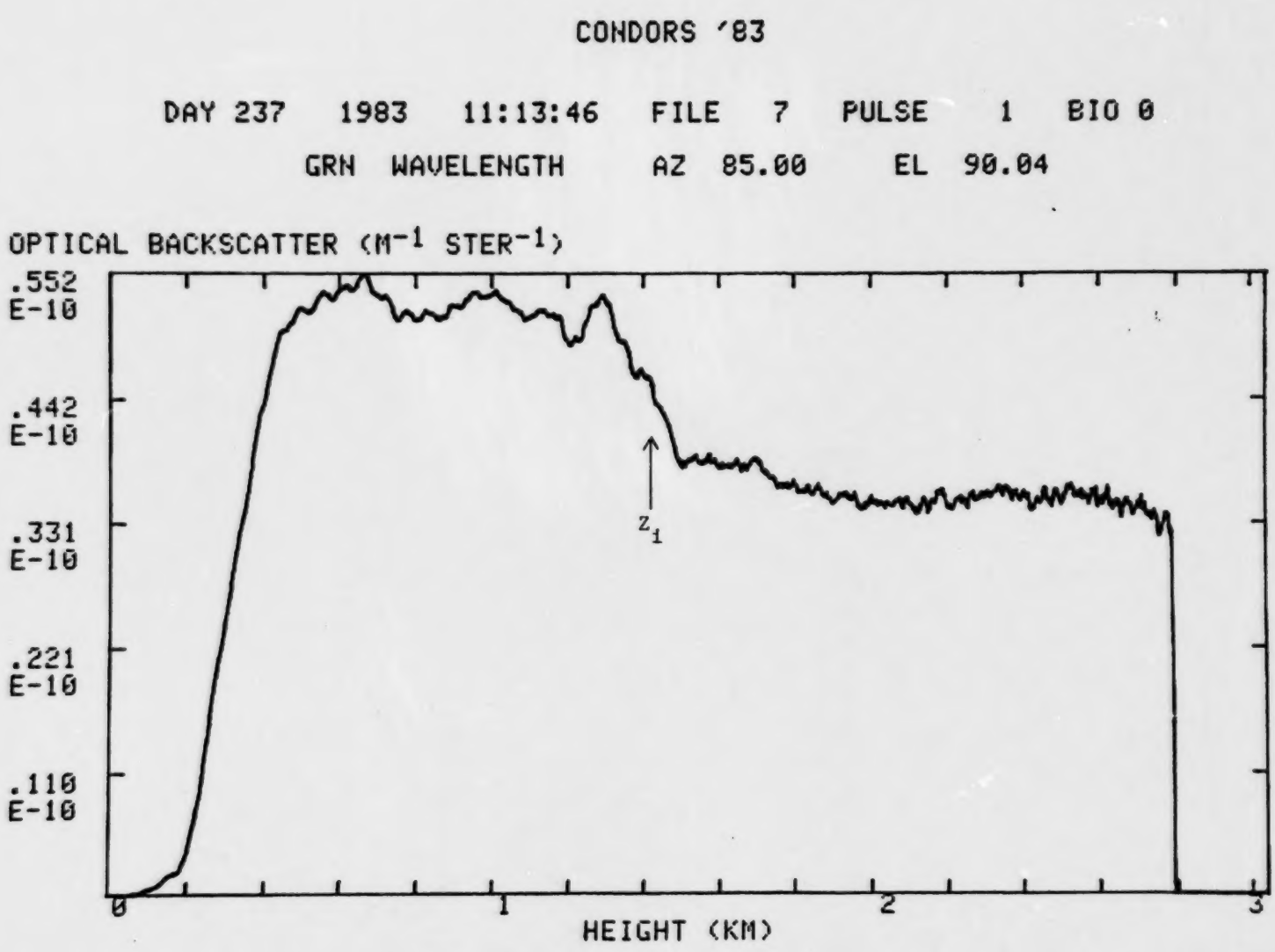

Fig. 9 Backscatter profile from the LIDAR system at 11:13 on 830825.

SECTION 5

ABL PARAMETERIZATION

Once the surface heat flux and stress and the inversion height are known, it is possible to estimate the windspeed, temperature, and turbulent velocity profiles based on similarity scaling laws. The scaling laws which will be used here are the surface-layer flux profile relations (Section 2), as well as turbulent velocity profiles derived from the Minnesota experiment (Caughey and Palmer, 1979), from aircraft measurements, and from laboratory water-tank studies (Willis and Deardorff, 1974).

The ABL windspeed and temperature profiles are assumed to follow their surface layer forms up to a height which for a given value of $-Z_i/L$ is a fixed fraction of the ABL height, and to be constant above that height. For large values of $-Z_i/L$ (as is the case for nearly all of the present data set, with $-Z_i/L \approx 200$ typically) the curvature of the profiles occurs at heights that are such a small fraction of Z_i that Z_i does not strongly affect the profiles; they can be extrapolated up to any height $-L \ll z \ll Z_i$. We found $0.2\ Z_i$ to give good results, although it makes little difference if 0.1 or 0.3 Z_i are used. For small $-Z_i/L$ values (say $\approx$ 1 to 20) $-L$ becomes such an appreciable fraction of Z_i that Z_i can become important in limiting the height to which the surface profiles can be extrapolated to. Because the $-Z_i/L$ values were so large in the present data set we were unable to critically test for this effect.

Based on the assumption of a well-mixed boundary layer, we simply assume that the mean wind direction is constant with height through the ABL. This value is taken as the mean wind direction at 10 m.

The ABL profiles of σ_u, σ_v and σ_w are based on the published results of Caughey and Palmer (1979) and of Willis and Deardorff (1974). The laboratory measurements of Willis and Deardorff are shown in Figs. 10a,b. This same data is plotted together with the Minnesota data by Caughey and Palmer in Figs. 11a,b.

The general characteristics of the $\sigma_{u,v}$ profiles are that they are nearly constant through the depth of the ABL, only increasing in the lowest 0.3 z/Z_i, and that the laboratory values are approximately only 50% of the atmospheric values. This is most likely due to the fact that the atmosphere is almost never horizontally homogeneous, but contains long term fluctuations of wind direction on a variety of scales. We can account for these large scale fluctuation by scaling the ABL profiles of $\sigma_{u,v}$ on their 10 m measured values. The parameterization

$$\frac{\sigma_{u,v}}{w_*} = C[0.5(2 - (z/Z_i)^{1/4}) + 0.1\ (z/Z_i)^2]^{1/2} \tag{56}$$

is also shown in Fig. 10b (as a dashed line) when a surface value of $C^2 = \sigma_{u,v_o}{}^2/w_*{}^2 = 0.5$ is used. This same curve is shown in Fig. 11b together with the Minnesota data.

The variance of vertical velocity profile is more nearly the same for the laboratory and atmospheric data (Figs. 10a, 11a). The parameterization

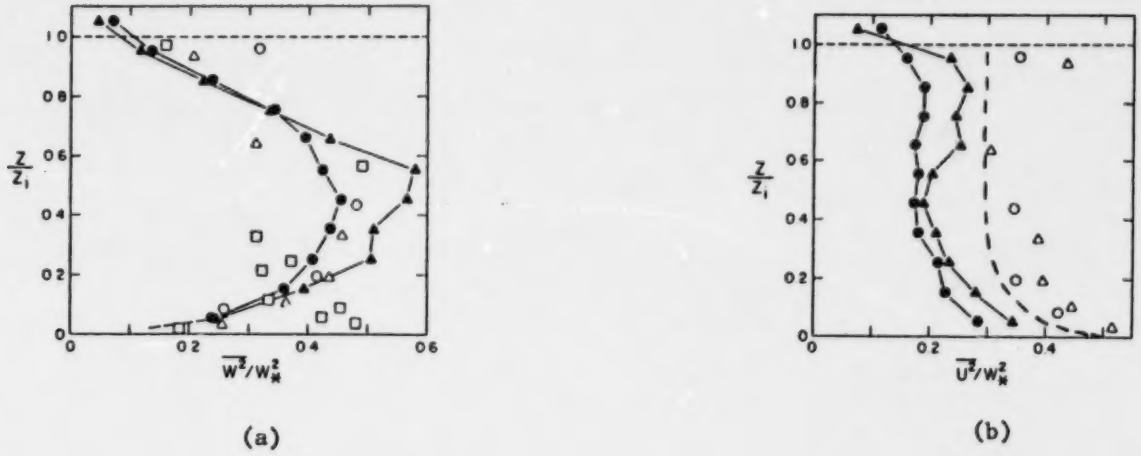

Fig. 10. Vertical profiles of dimensionless vertical (a) and horizontal (b) velocity variance (Willis and Deardorff, 1974). Solid symbols denote laboratory tank data, open symbols denote aircraft data. dashed curve in (b) is from enq.(52) using C = 0.5.

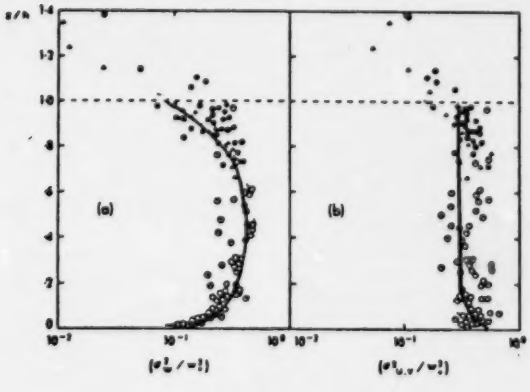

Fig. 11. As in Fig. 10, with atmospheric data from Caughey and Palmer (1979). Solid curves are based on Eqns. (56-57) of the text.

$$\sigma_w/w_* = [1.8(z/Z_i)^{2/3}\ (1 - .91\ (z/Z_i))]^{1/2} \qquad (57)$$

is seen in Fig. 11a to be a reasonable fit to both sets of data. This form also reduces to the free-convection prediction for σ_w as z/Z_i approaches zero.

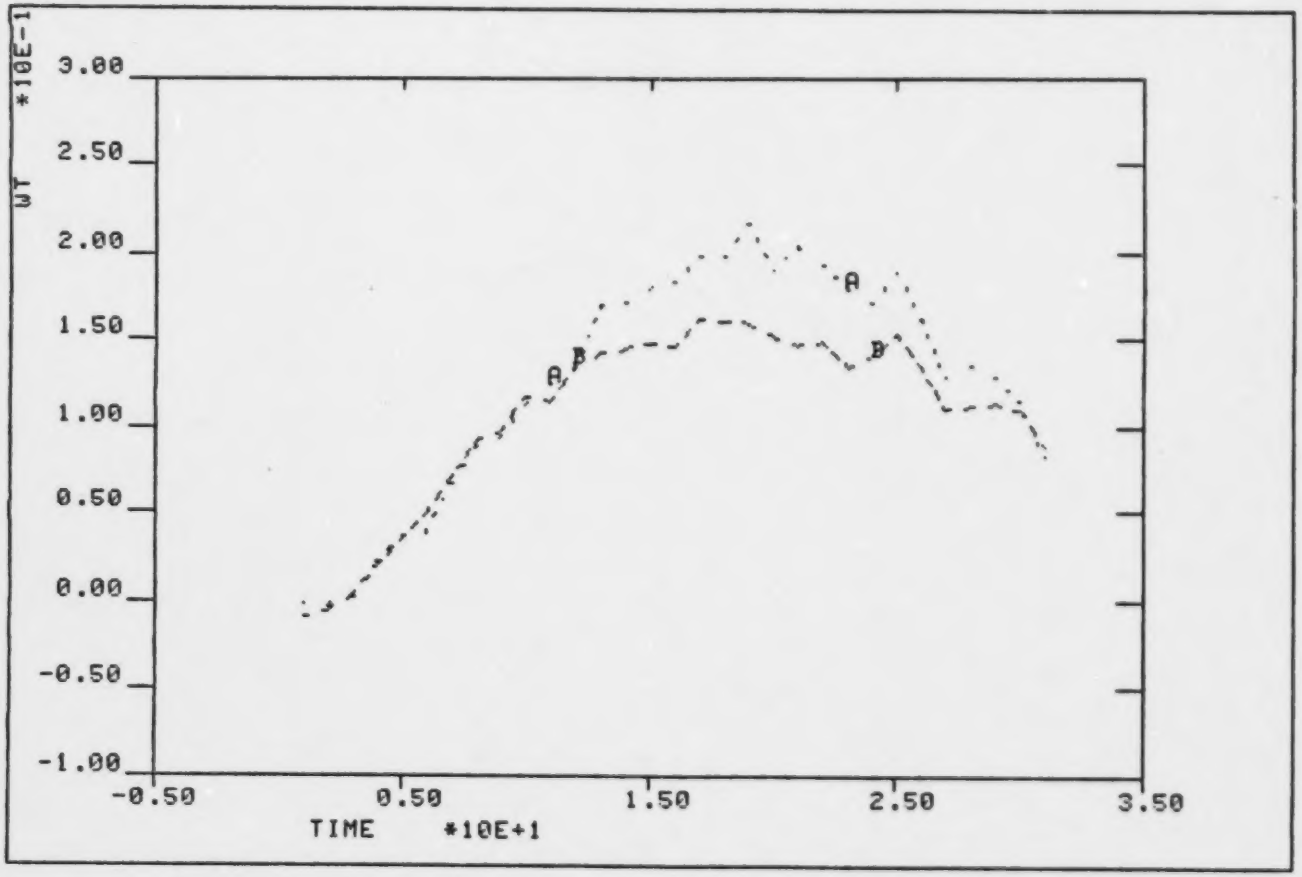

Fig. 12. Ensemble averages of surface heat flux for 26 days of data as a function of time from sunrise. Curve A represents the measured values, curve B values derived from the Kansas flux-profile equations.

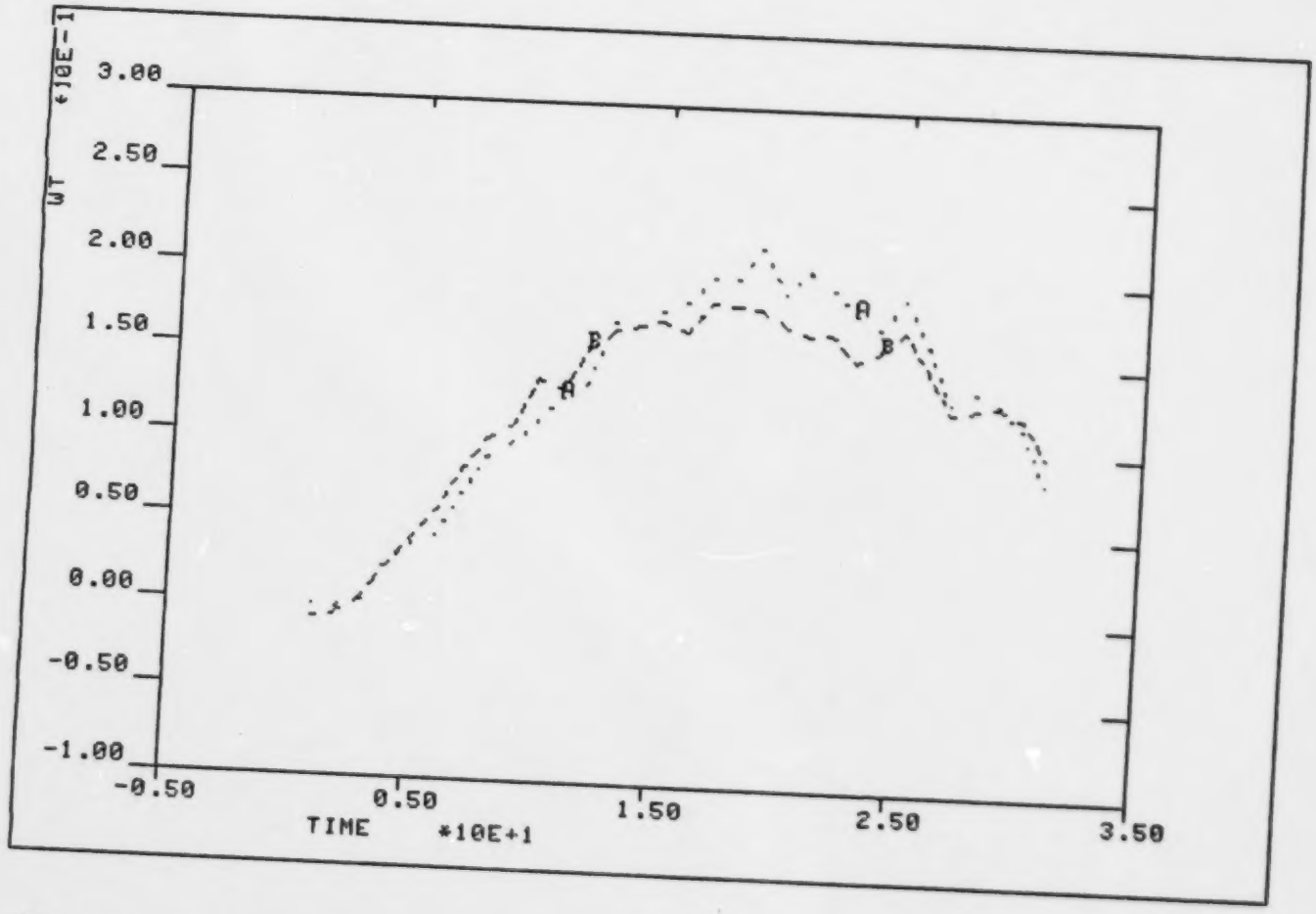

Fig. 13a. As in Fig. 12, except the calculated heat flux is derived from the ITCE flux-profile equations.

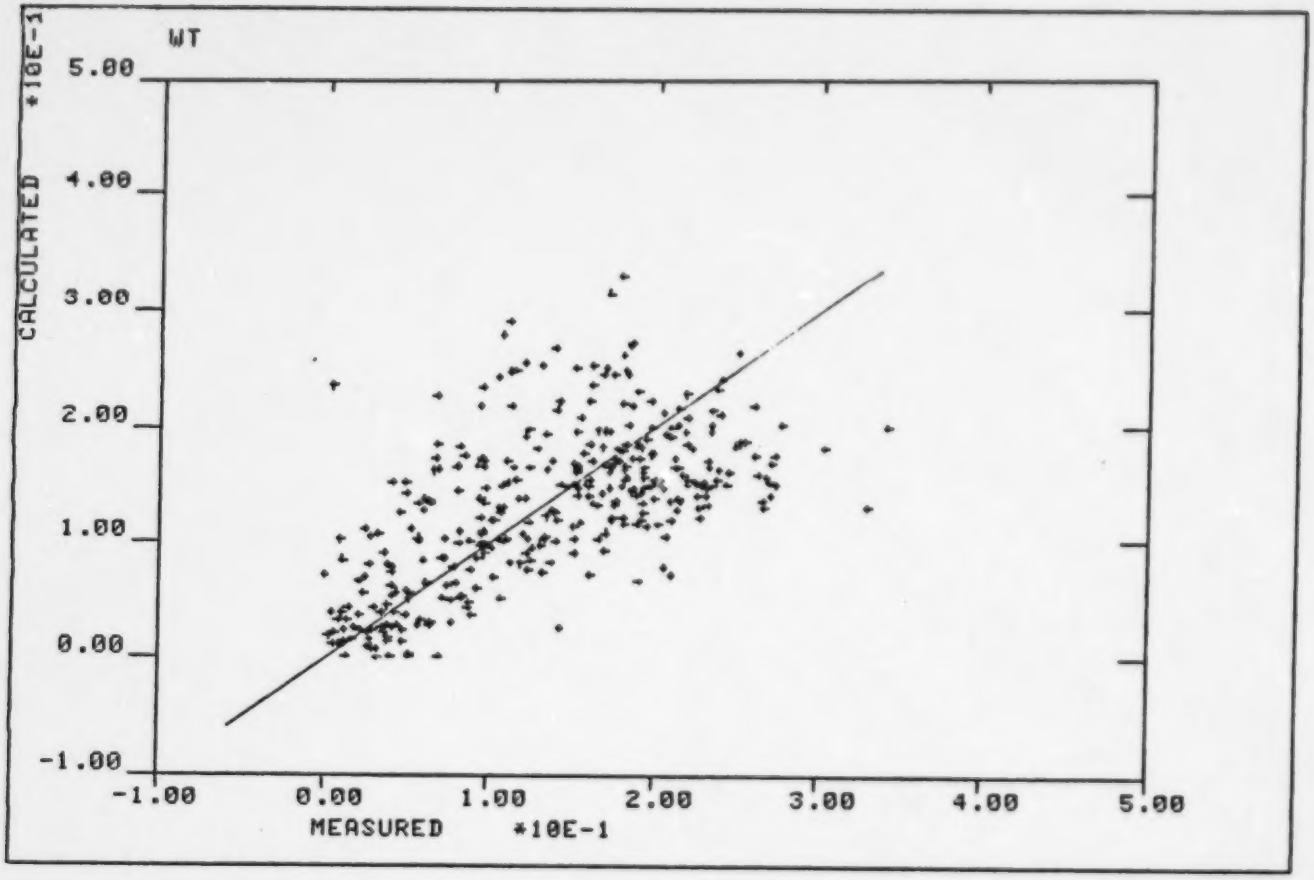

Fig. 13b. Predicted and measured 20 minute values of surface heat flux.

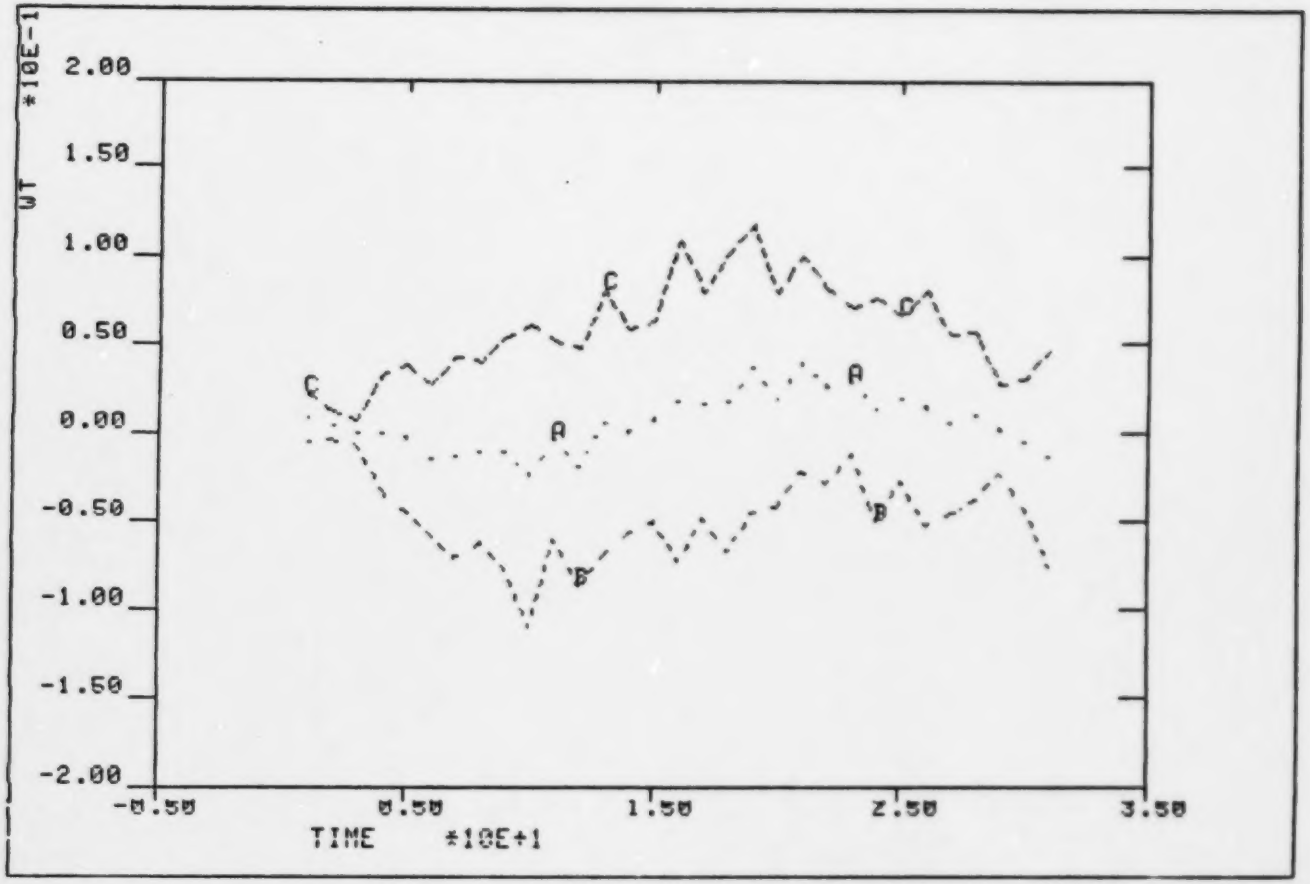

Fig. 13c. Ensemble mean bias and error of the predicted heat flux. Curve A represents the mean bias, curves B and C are the bias ± one standard deviation.

Because of this better agreement, ITCE derived values of surface fluxes will be used henceforth.

Individual 20 min values of calculated and measured heat flux are compared in Fig. 13b. This figure shows that although the ensemble values are in close agreement, considerable differences exist between individual values. This is further demonstrated in Fig. 13c; here curve A represents the mean bias, or difference between the ensemble measured and calculated values,

$$A = \frac{1}{n} \sum_{i=1}^{n} \delta_i = \bar{\delta} \tag{58}$$

where δ_i = measured value - calculated value. (59)

Curves B and C are ± one standard deviation relative to the mean bias, given by

$$B,C = A \pm \left[\frac{1}{n-1} \sum_{i=1}^{n} (\delta_i - \bar{\delta})^2\right]^{1/2} . \tag{60}$$

Comparing Figs. 13a and 13c we see that one standard deviation is roughly 50% of the measured heat flux.

The ensemble stress calculated from the ITCE profiles is shown in Fig. 14a which shows good agreement between calculated and measured. In contrast to the heat flux, little difference was found between the stresses calculated using the Kansas and ITCE profiles. The scatter plot of stress, Fig. 14b, shows a larger spread than the heat flux. In fact, 26% of the points actually have a positive measured stress. Figure 14c shows that the standard deviation of the difference between measured and calculated relative to the mean bias is 100% or more of the actual stress. Because so many of the measured stresses are positive, for which the Obhukov length L is undefined, we do not compare calculated and measured values of L.

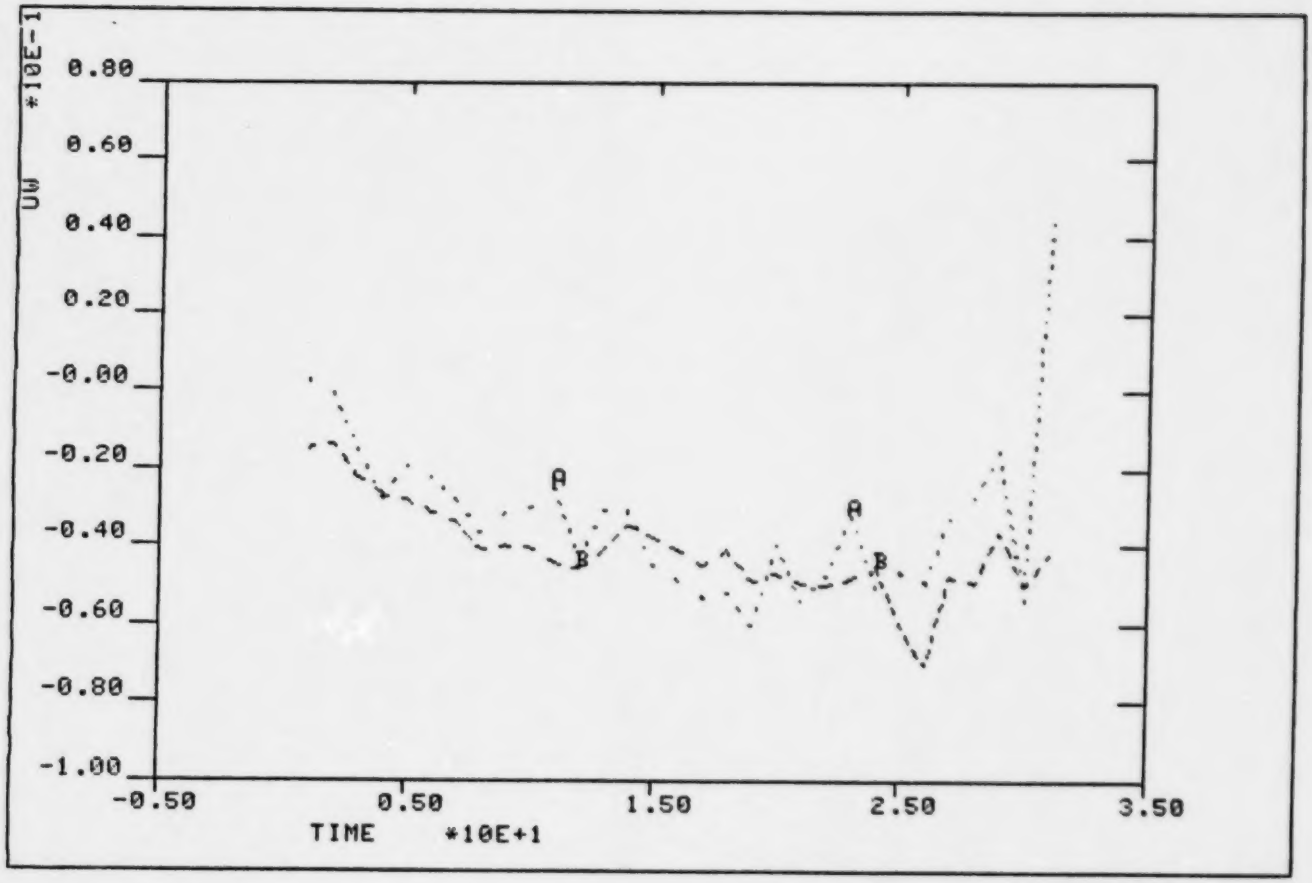

Fig. 14a. Ensemble averages of surface momentum flux. Curve A represents measured values, curve B calculated values.

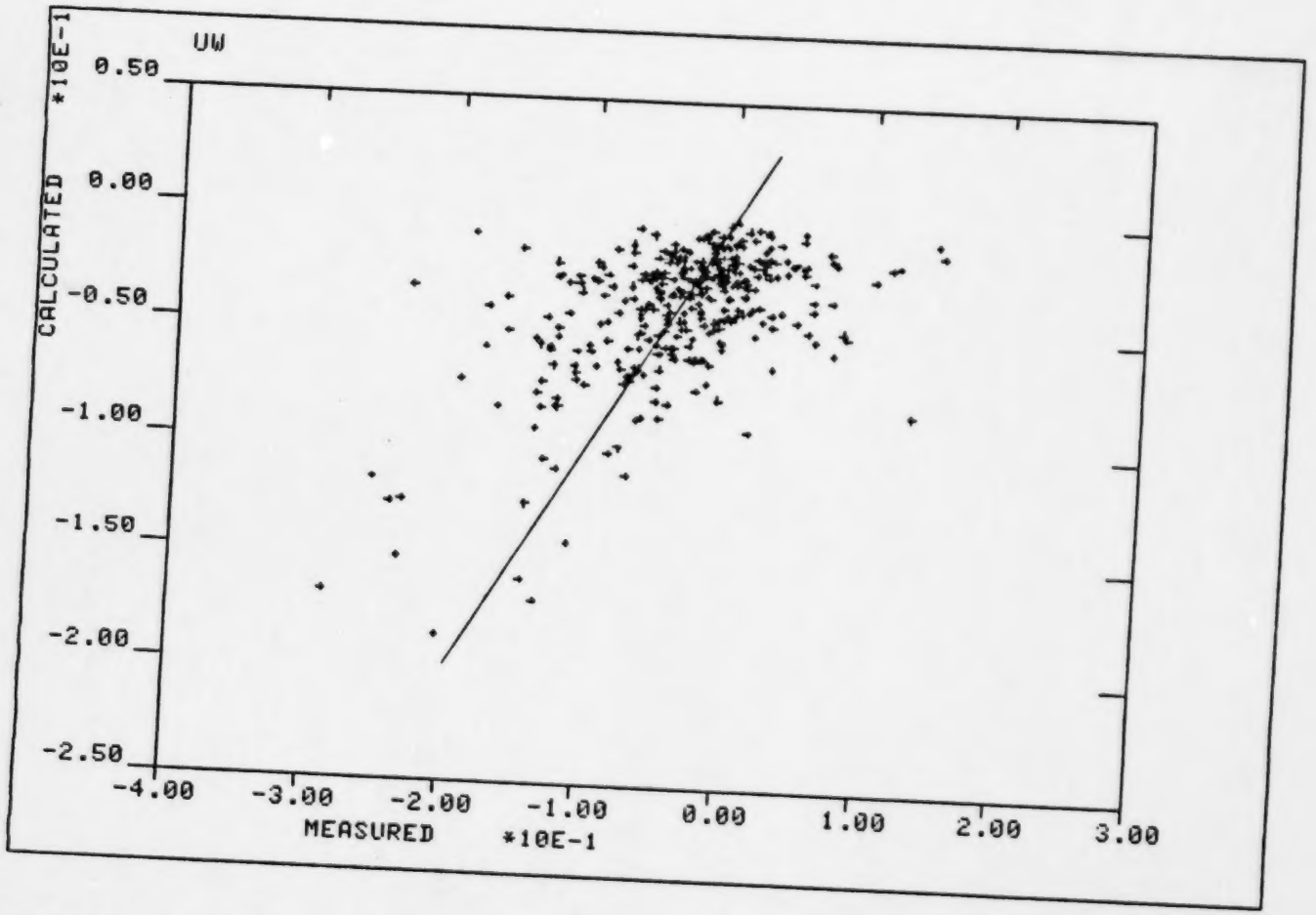

Fig. 14b. Predicted and measured 20 minute values of surface momentum flux.

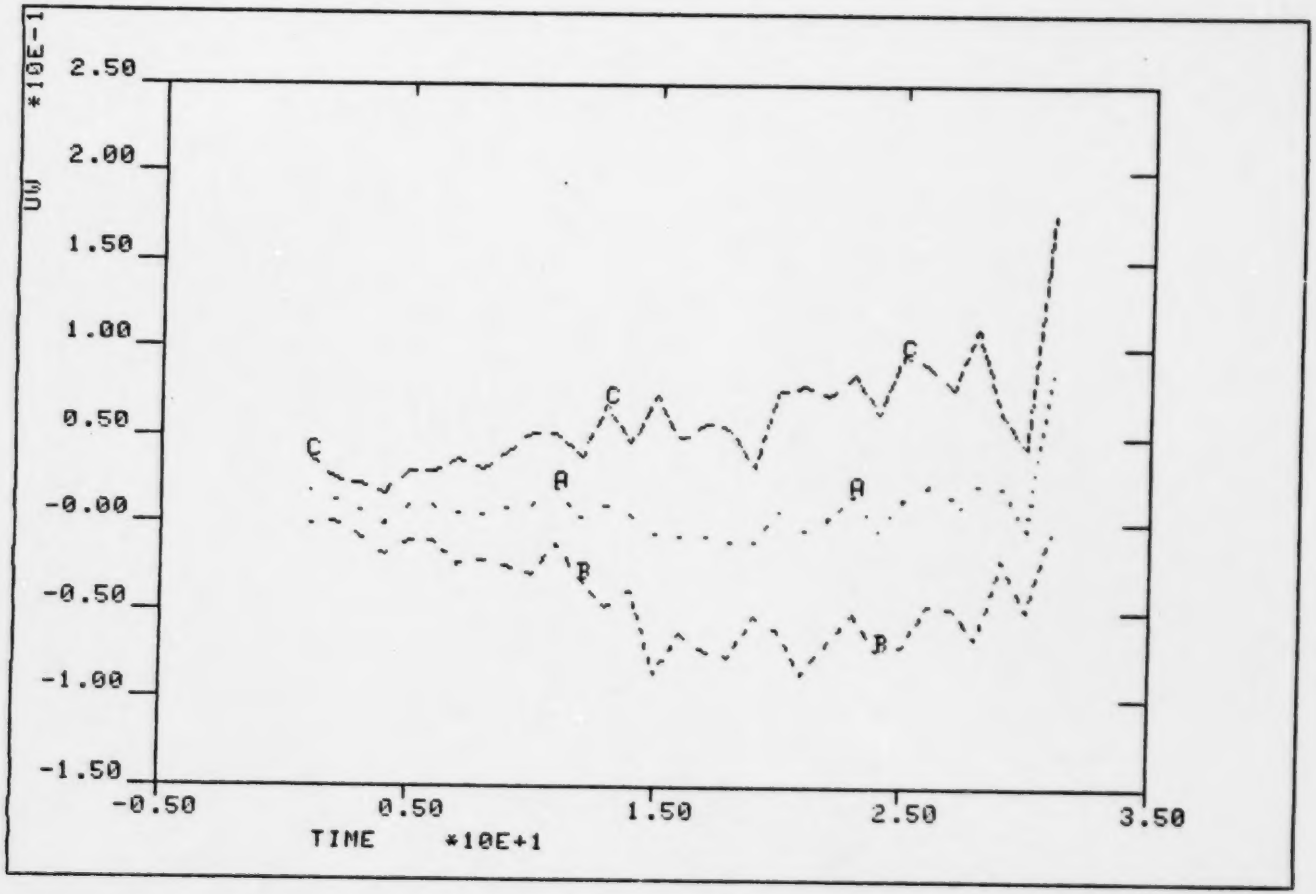

Fig. 14c. Ensemble mean bias and error for the predicted momentum flux. Curve A is the bias, B and C are the bias $\pm$ one standard deviation.

There are several possible sources of error which might account for the large differences between individual 20 min calculated and measured values. Five obvious sources are (1) instrumental failure or miscalibration; (2) an incorrect formulation of the flux profile relationships; (3) an incorrect surface roughness value; (4) errors due to the turbulence being non-stationary and/or inhomogeneous; (5) sampling errors due to the 20 min averaging period being insufficient to get a true representation of the mean and turbulent fields.

The first of these sources of error, instrumental failure or miscalibration, is unlikely to be an important factor. The data set was carefully edited to eliminate periods when instruments showed signs of improper behavior. Also, the quality and calibration accuracy of the BAO instruments are most likely equal to if not better than the instruments used to derive the flux-profile relations themselves.

An incorrect formulation of the ITCE flux-profile relations is also unlikely to be a large source of the 20 min differences, because the ensemble value of heat flux and stress (Figs. 13a and 14a) are in close agreement. For the 20 min values to be substantially different but the ensemble values to be in good agreement would require a fortuitous combination of periods of the flux-profiles consistently incorrectly underestimating and then overestimating the fluxes. For the same reason one can rule out either a consistently high or low value of surface roughness. It is possible however, that z_o changing as a function of time or direction could account for some of the 20 min scatter.

Errors due to the flow being non-stationary and/or inhomogeneous are surely present, because no attempt was made to select only "ideal" conditions. The magnitude of these errors is however very difficult to assess.

The last category is referred to as "sampling error". These are errors due to the fact that a 20 min value may not represent a true ensemble value of the turbulent flow. Since longer averaging times are required for higher order moments (Wyngaard, 1971) we expect that $\overline{U}$, $\overline{\theta}$, and $\overline{\theta_2}$ have greater accuracy than $\overline{w'\theta'}_m$ and $\overline{u'w'}_m$. Since the calculated heat flux and stress are derived from $\overline{U}$, $\overline{\theta_1}$ and $\overline{\theta_2}$, it is likely that the calculated fluxes are a better representation of the true surface fluxes than the 20 min measured values are. To estimate the effects of averaging time we also computed fluxes using hour values of $\overline{U}$, $\overline{\theta_1}$ and $\overline{\theta_2}$ and compared them to hour long measured values (Fig. 15a,b). For heat flux the standard deviation was reduced to 30%, while for stress it was reduced to less than 70%. Since most of the runs in this data set had small wind speeds, which require long averaging times (the average 10 m wind speed was only 1.8 m s^{-1}), it is likely that a significant portion of the remaining variance is still due to insufficient averaging time.

Having the calculated values of the surface fluxes, the inversion growth can now be predicted using the methods developed in Sec. 3. Two examples of the inversion rise prediction and measured values of Z_i are given in Figs. 16a,b. In Fig. 16b we see that differences as large as 200 m can be found between Z_i obtained from the different measurement systems. This is principally due to the fact that both the lidar and rawinsondes measure point values of Z_i, which can be a highly variable function of location and time.

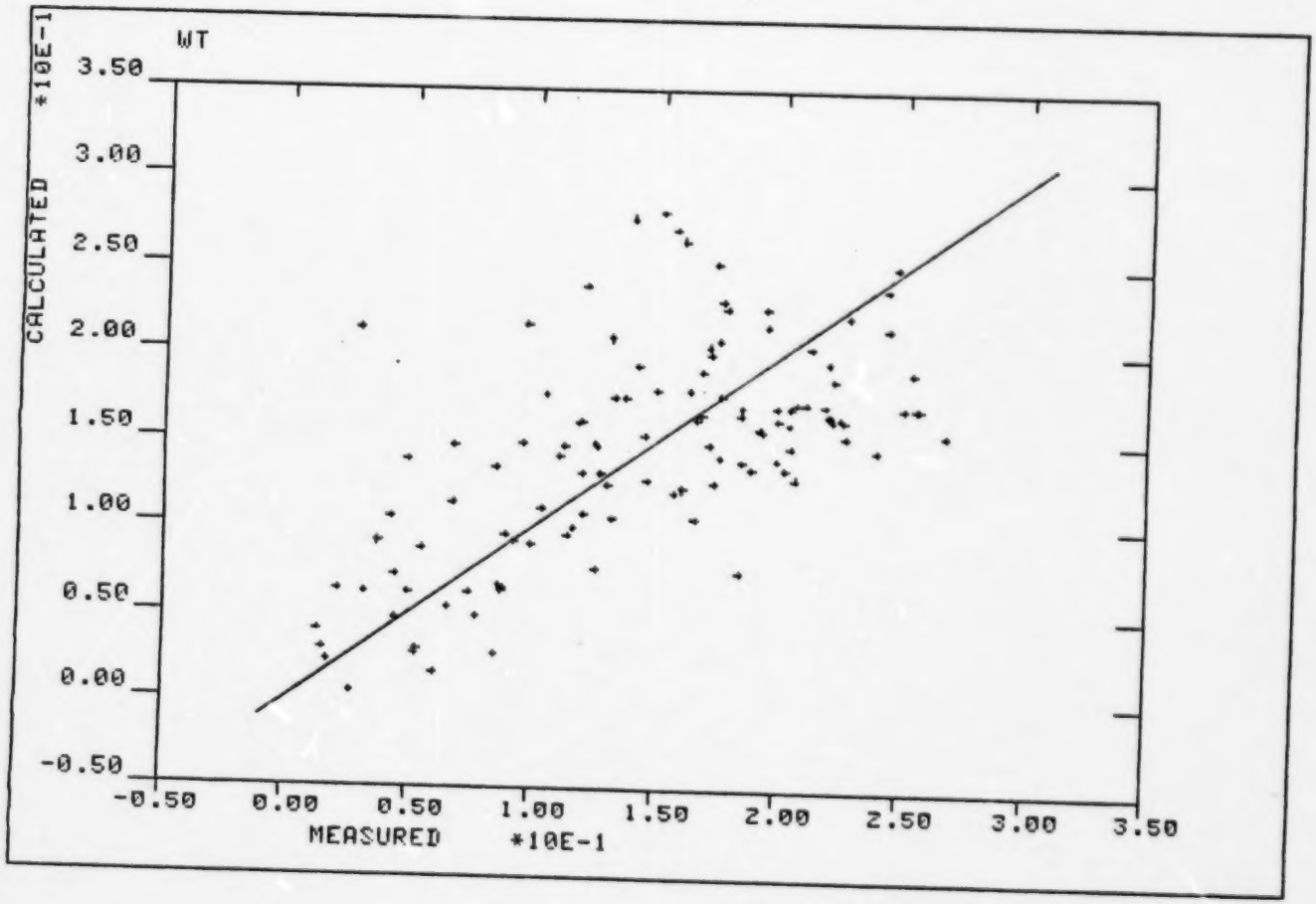

Fig. 15a. Predicted and measured hour averaged values of surface heat flux.

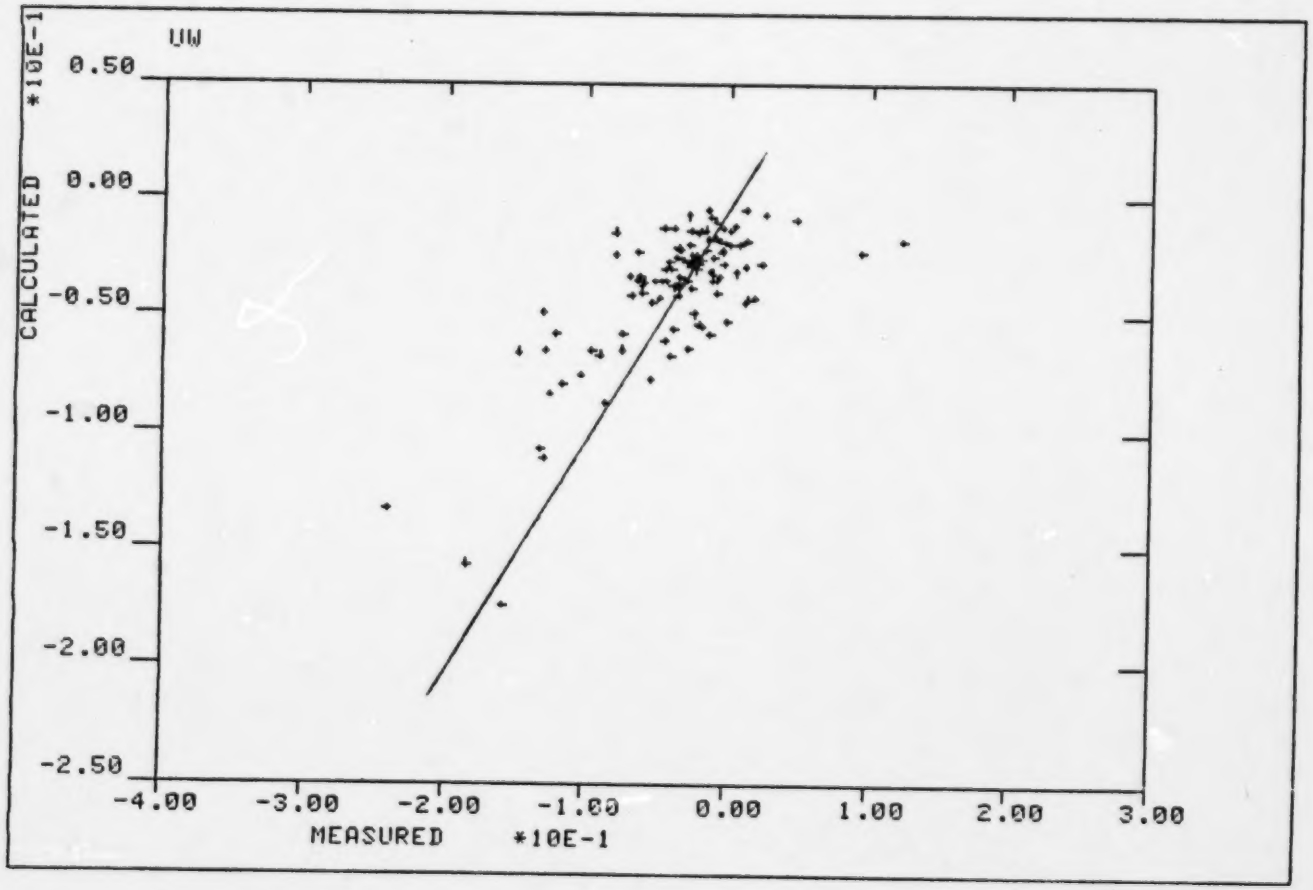

Fig. 15b. Predicted and measured hour averaged values of surface momentum flux.

Individual values of Z_i are presented as a scatter plot in Fig. 17a, while ensemble values of the measured and calculated inversion heights are given in Fig. 17b. Again, only periods when both measured and calculated values are available are included in the ensemble. For most of the day, the calculated ensemble Z_i agrees with the measured value to within better than 10%, with differences less than 50 m. Only at approximately 8 hours after sunrise does the calculated value begin to diverge, with it being smaller than the measured Z_i. The significance of this is not clear however, because there are many fewer points to be averaged together this late in the day. The standard deviation between the measured and calculated Z_i's relative to the mean bias is given in Fig. 17c. The error increases as Z_i increases, remaining approximately 30% of Z_i throughout the day. A large part of this error is likely to be due to the fact that point measurements of Z_i are made (as discussed above). Also cold or warm air advection will change the lapse rate γ, causing inaccuracies in the calculated inversion heights. Finally, accumulated errors in the 20 min calculated surface fluxes will add to the error in Z_{i_c}.

The inversion rise equations also predict the mean ABL potential temperature, θ_{BL}, as a function of time. We plot the calculated vs. measured values in Fig. 18a, together with slopes of 1 to 1 and 2 to 1. The "measured" values are calculated by averaging $\overline{\theta}(z)$ from all tower levels with $0.2 < z/Z_{i_m} < 0.8$. Interestingly, the calculated values start off for each day with an $\approx$ +1°C bias relative to the measured, follow a 1 to 1 slope for several hours after sunrise, then increase at a rate only about one-half of the measured rate until θ_{BL_m} is 2° to 3°C warmer than θ_{BL_c}, and then finally return to a 1

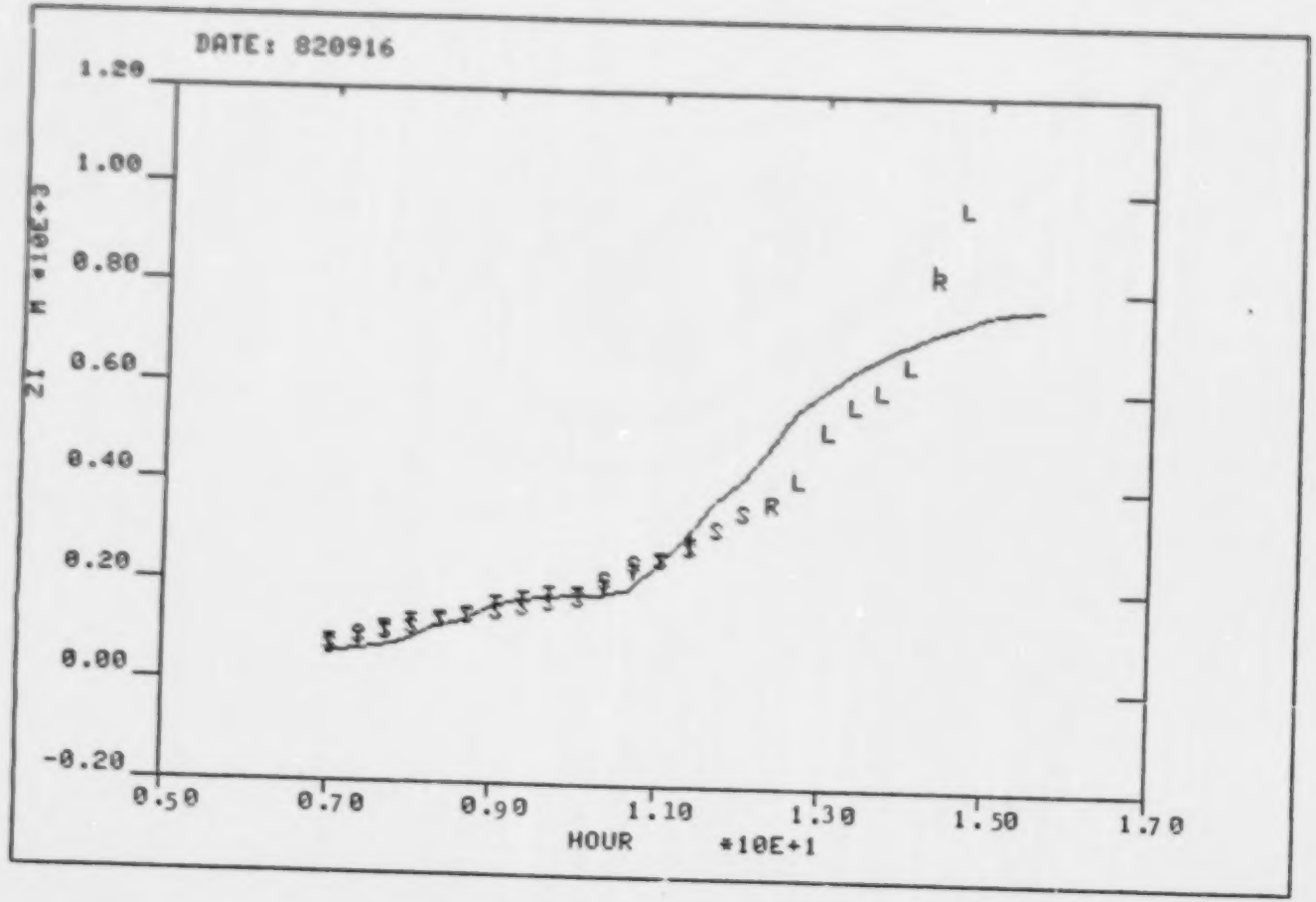

Fig. 16a. Predicted and measured values of Z_i on 820916. Tower measurements are denoted by T, sodar by S, lidar by L, and rawinsonde by R.

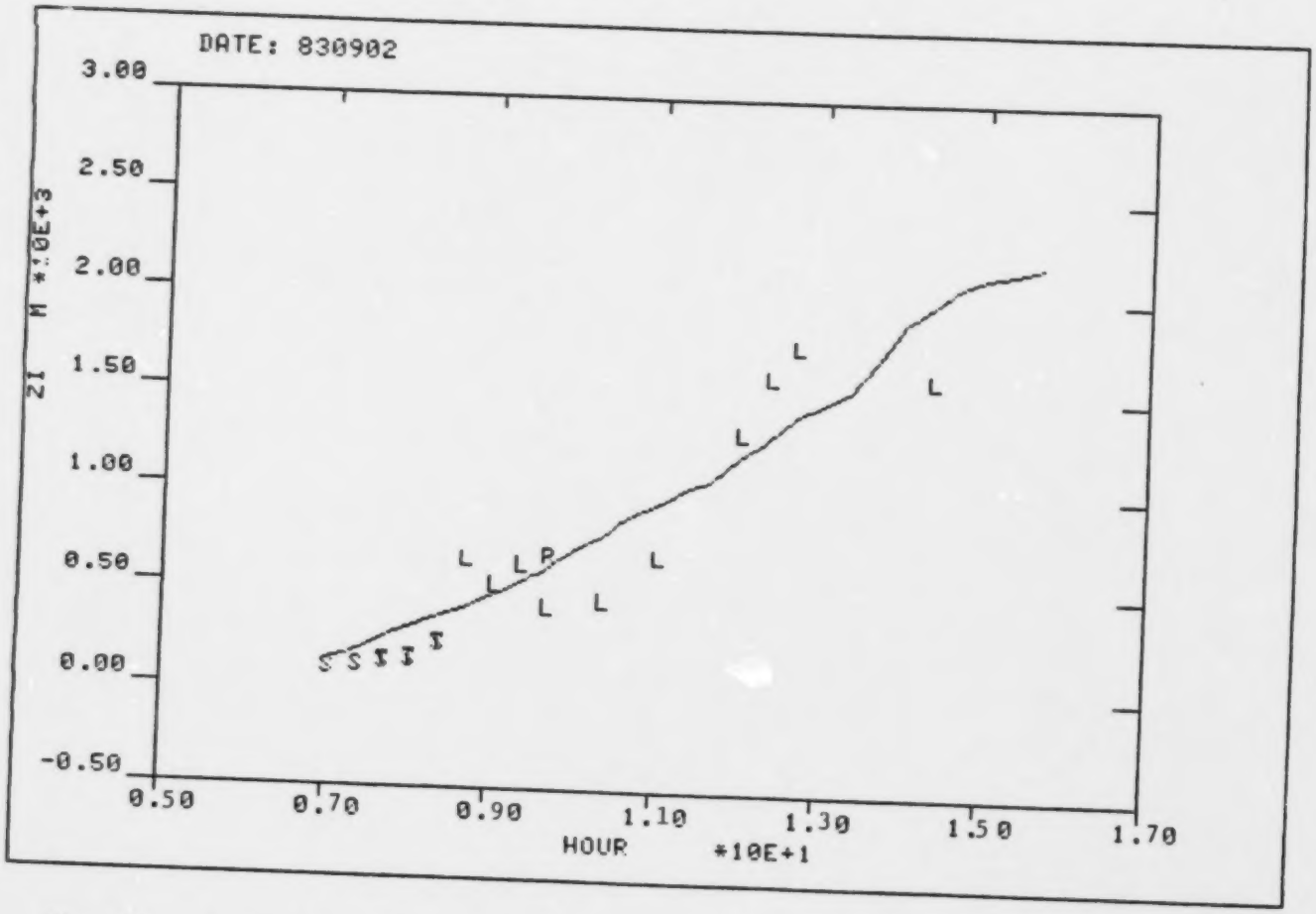

Fig. 16b. As in Fig. 16a, except for 830902.

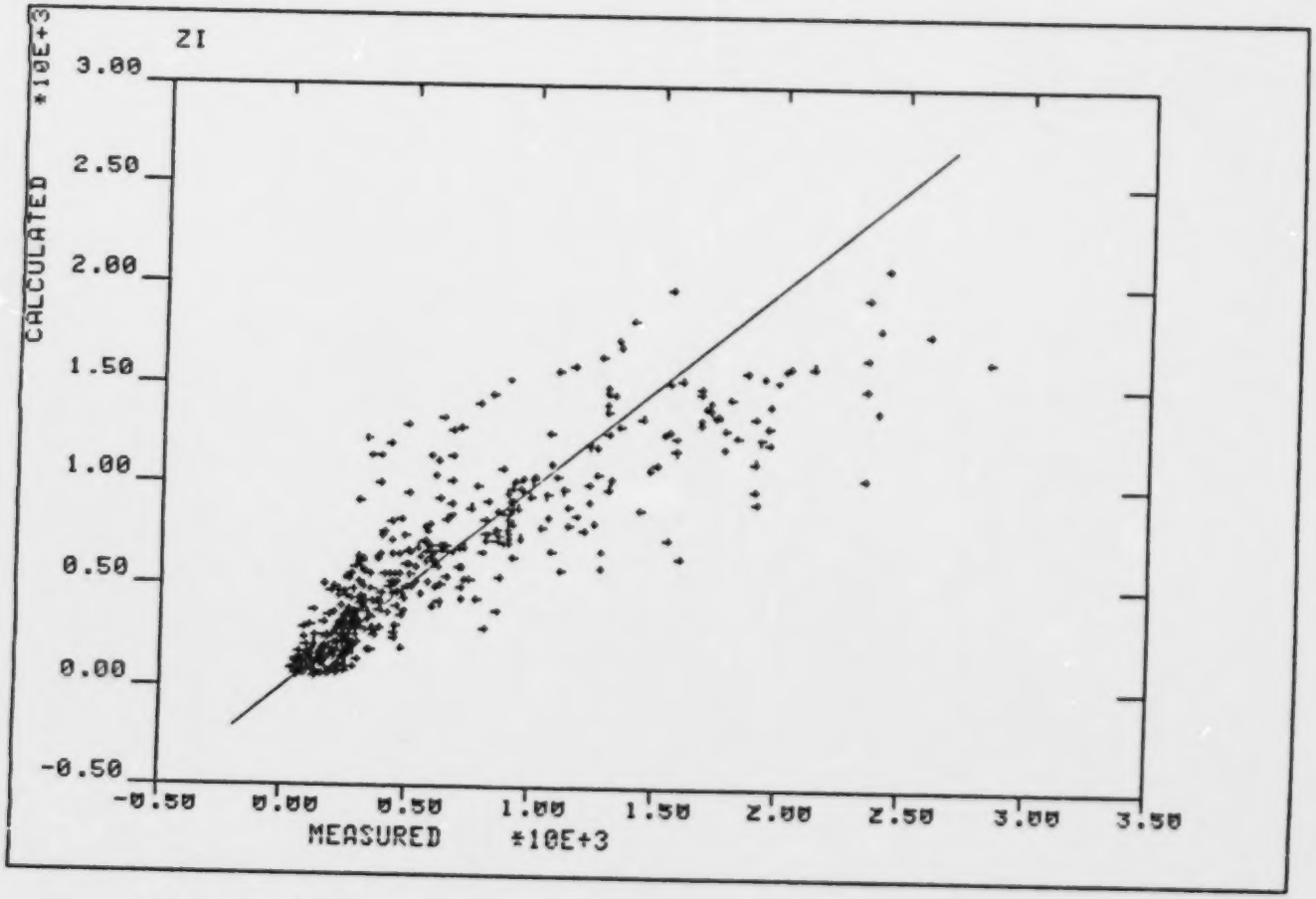

Fig. 17a. Calculated and measured values of the inversion height.

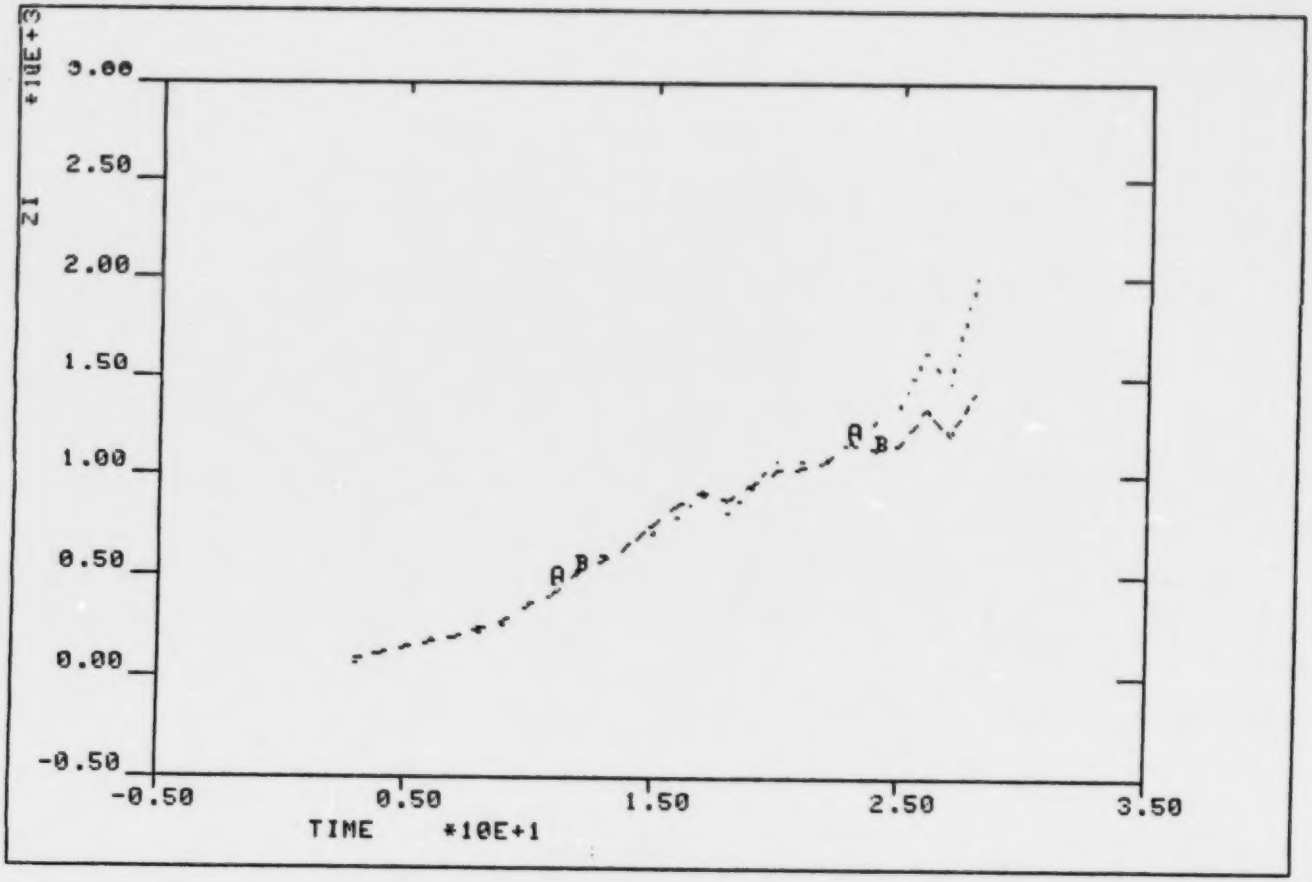

Fig. 17b. Ensemble averages of measured (curve A) and calculated (curve B) inversion heights as a function of time from sunrise.

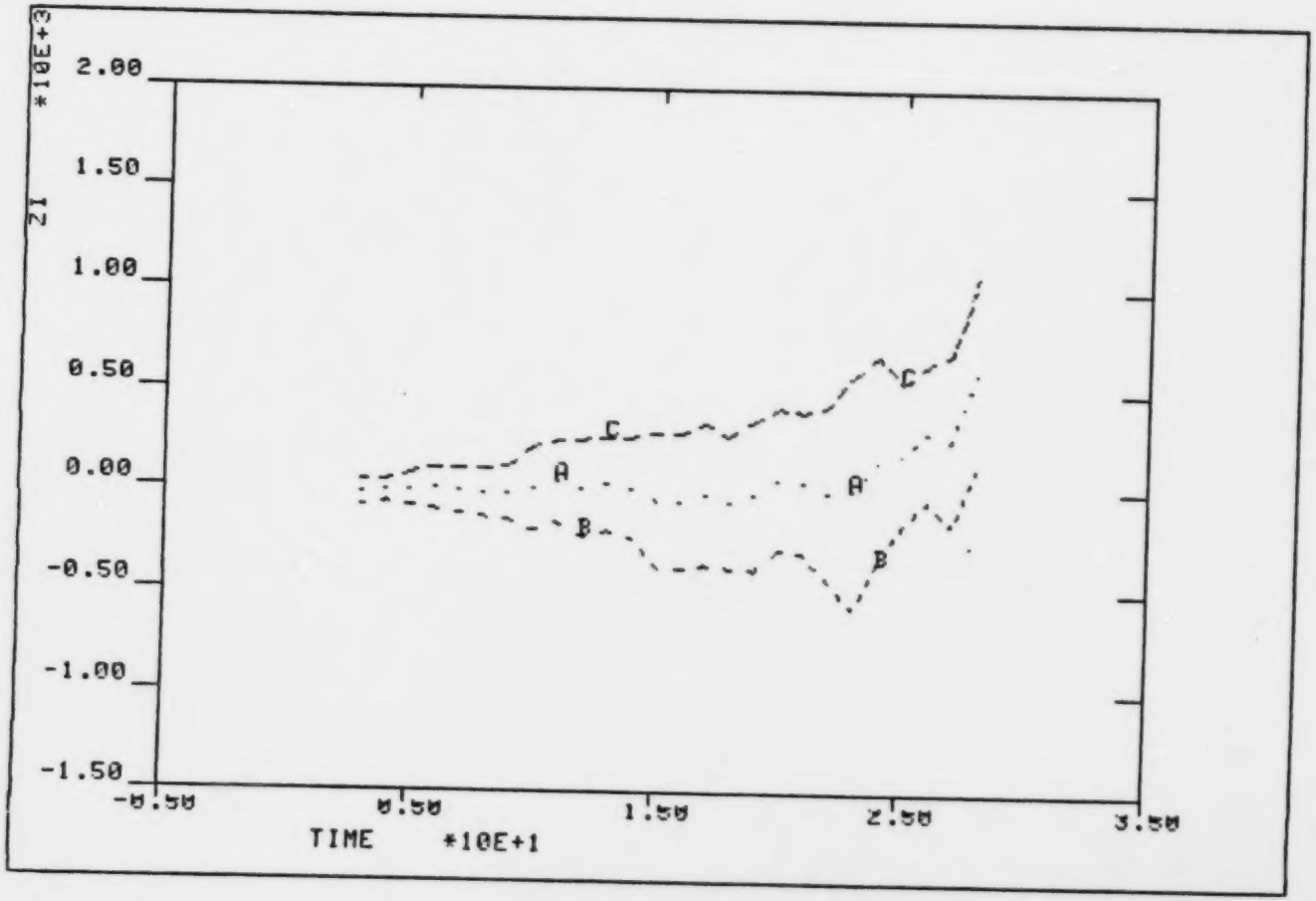

Fig. 17c. Ensemble mean bias (curve A) and error of the inversion height, as a function of time from sunrise.

to 1 slope in the late afternoon. The net result is a series of "S" shaped curves, each displaced according to the value of the initial morning temperature. Ensemble values of θ_{BL} are plotted vs. time in Fig. 18b, which again shows the change in bias between calculated and measured from morning to late afternoon.

Since the prediction of Z_1 and θ_{BL} are derived from a set of coupled equations, it is surprising for the first prediction to do well, while the latter prediction displays such consistent but unexplained behavior.

Nearly all of the radiosonde ascents used as input to the inversion rise model were taken within 15 minutes of sunrise. This makes any additional radiational cooling an unlikely source of the cooler measured values during early morning. More likely this is an effect of the BAO (and radiosonde launch site) being located on a slight knoll (Fig. 2) with the terrain dropping off by ≈50 m in a distance of 4 km to the west, north and east. This will result in cooler pools of air surrounding the BAO at sunrise. As this air begins to be mixed together in a developing convective ABL, the measured temperature will be cooler than the calculated temperature.

There are several possible causes for the more rapid heating of the boundary layer relative to the model prediction that follows. First there is horizontal advection. With a mean wind speed of 2 m s^{-1} and a warming of 4°C over 6 hours, this would require a horizontal temperature gradient of ≈4°C/45 km. We hope to check for consistent horizontal temperature gradients ($\overline{\theta}$ increasing to the east) in the PROFS mesonet data, which consists of approximately 25 surface stations in a 100 × 100 km area surrounding the BAO.

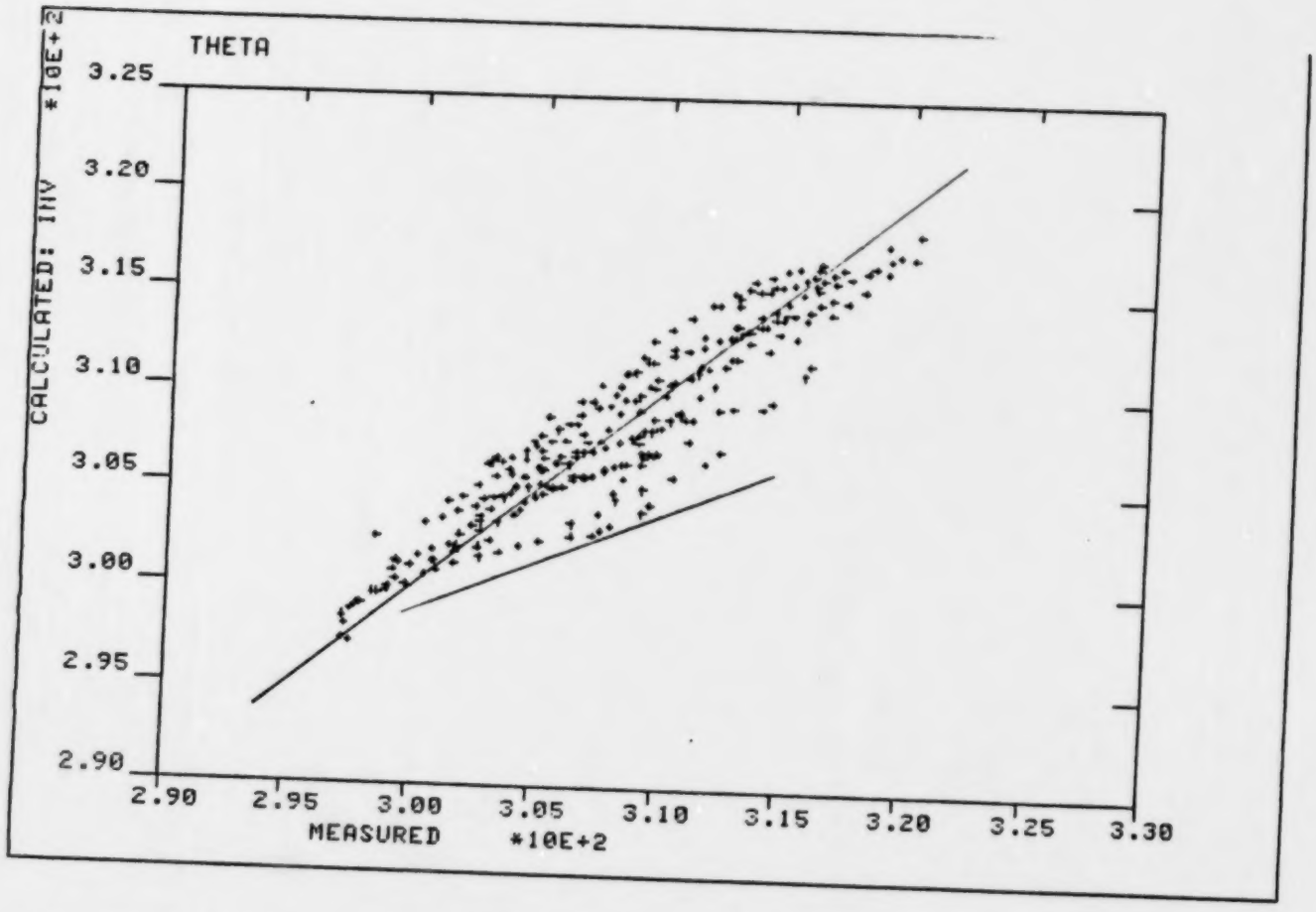

Fig. 18a. Mixed layer temperatures predicted from the inversion rise model vs. measured values.

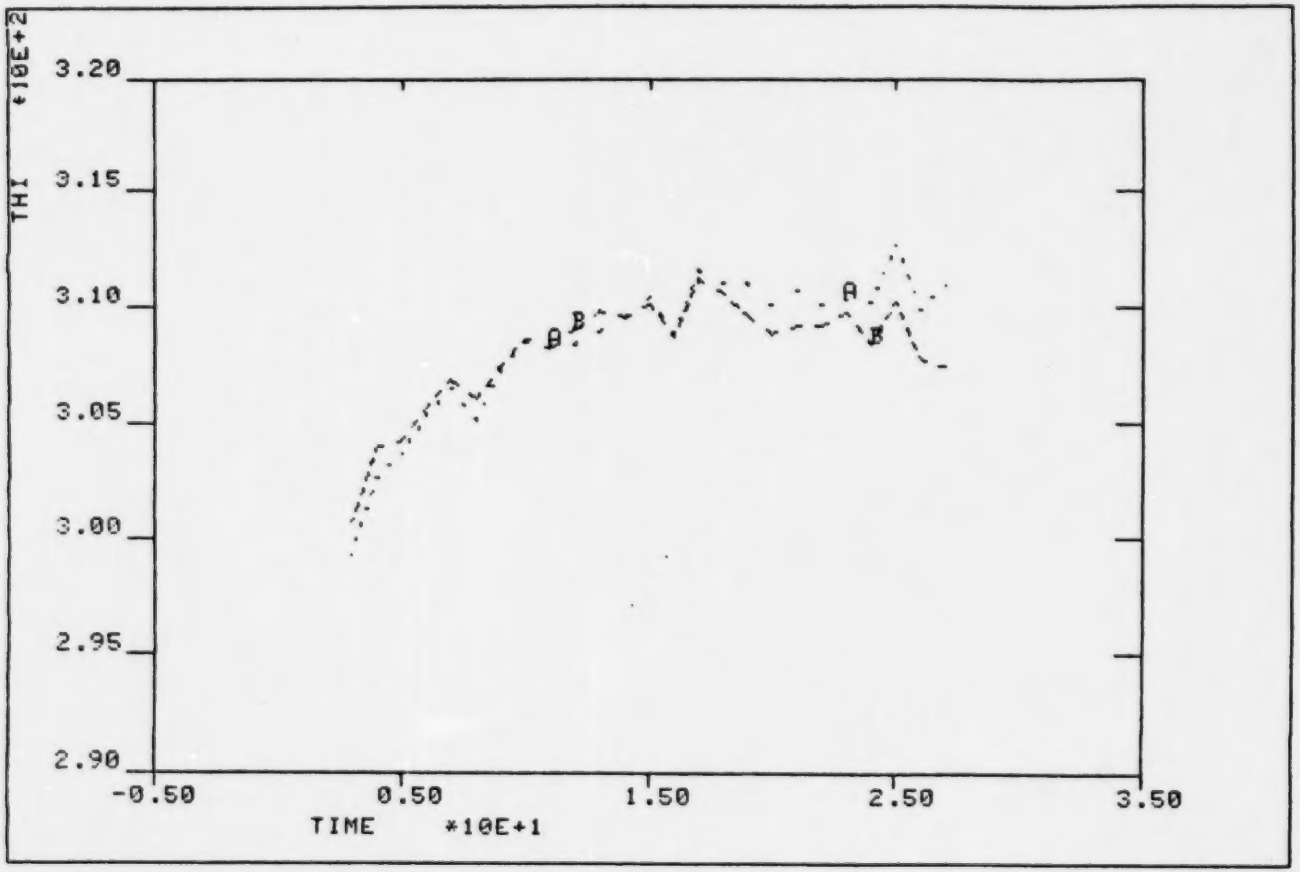

Fig. 18b. Ensemble averages of measured mixed layer temperatures (curve A) and inversion rise predicted values (curve B) as a function of time from sunrise.

A second source of the large measured θ_{BL} could be a combination of large-scale subsidence and inversion layer shear. At present the inversion rise model only has surface heating and stress as its driving forces. Shear across the inversion will also increase entrainment, thereby increasing Z_i and θ_{BL}. However, if there is large-scale subsidence present, its effect on Z_i could balance out inversion shear induced growth while θ_{BL} increases. Since the lower ABL consists of thermally forced upslope flow, we know strong shear exists within the ABL; also, the upslope flow is likely to be forced back at upper levels after it reaches the Front Range, which would result in an additional subsidence over the plains to augment the synoptic scale subsidence present on these mostly clear-sky days.

Having calculated values of the surface fluxes and of Z_i, profiles of mean and turbulent quantities were then predicted for the ABL. The first of these profiles is the mean potential temperature. Since the ABL is well-mixed, we assume that $\overline{\theta}(z)$ follows the surface layer profile up to $z = \alpha Z_{i_c}$, where $\alpha = 0.2$, and is constant above that level. For the present data set, the actual profiles are not very sensitive to the value of α used. This is because -L is small while $-Z_i/L$ is very large (on the order of 200), so that most of the gradient of $\overline{\theta}$ occurs for $z \lesssim .01\ Z_i$. At greater heights the $\overline{\theta}$ profile is essentially flat, and it makes little difference how high it is extrapolated to. For small values of $-Z_i/L$ (which are generally absent from the present data set) the value of α may in fact be different.

An example scatter plot of temperature difference at the 150 m level is given in Fig. 19a while the ensemble ABL profile of $[\overline{\theta}(z) - \theta(2\ m)]/\theta_{*_c}$ vs. z/Z_{i_m} is shown in Fig. 19b. The PBL profiles are determined by dividing $0 < z/Z_{i_m} < 1$ into 13 bins separated at heights of .025, .05, .1, .15, .2, .3,

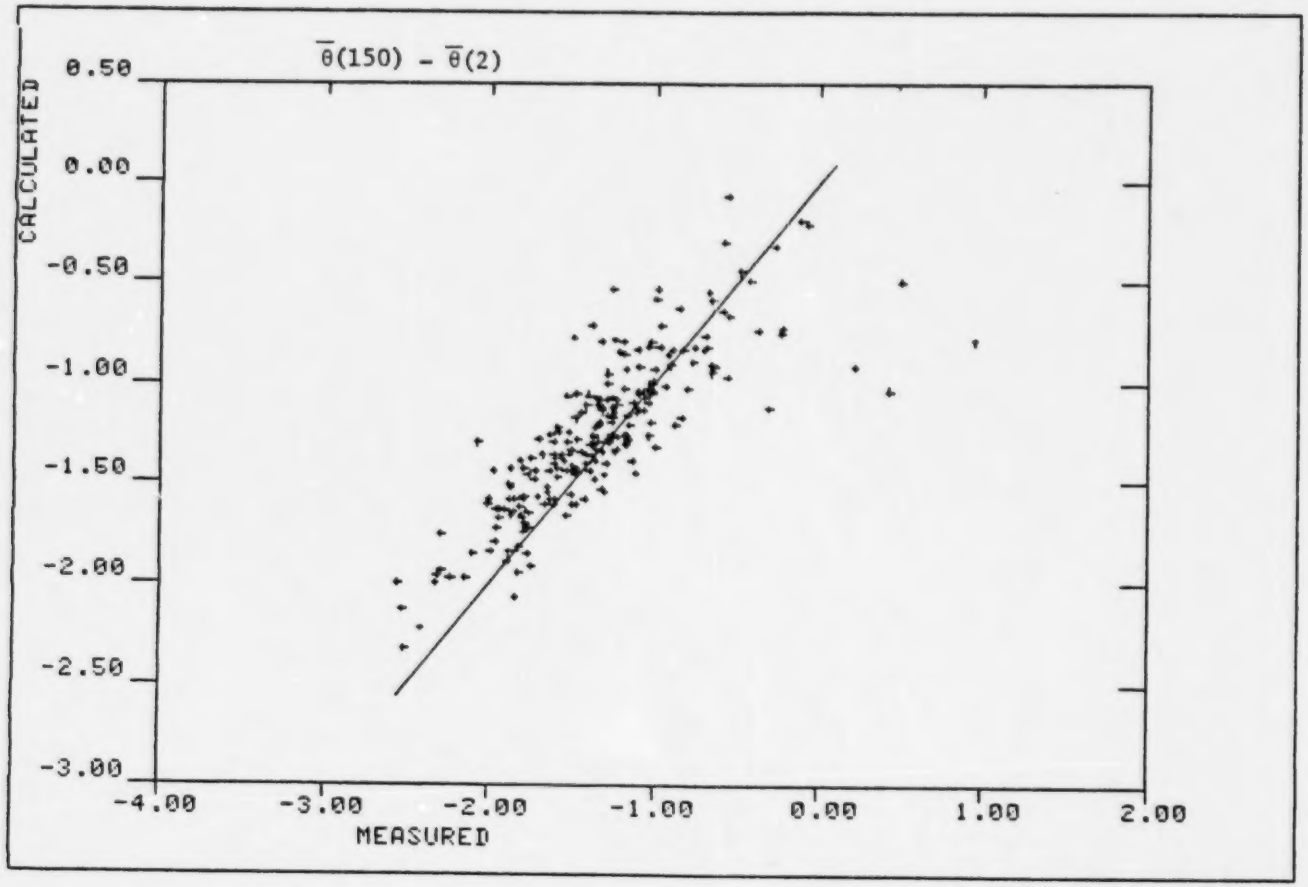

Fig. 19a. Calculated and measured potential temperature differences between z = 150 m and z = 2 m.

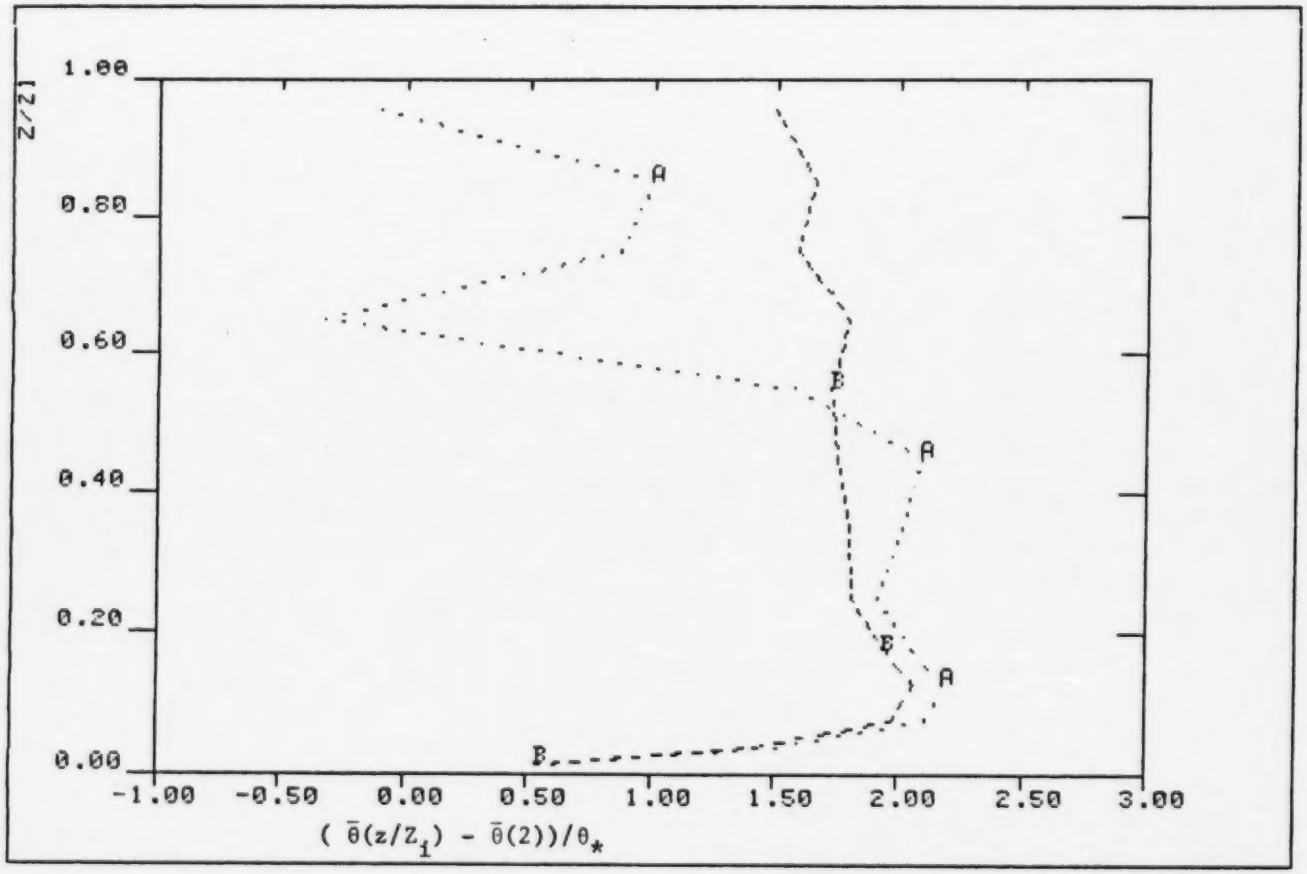

Fig. 19b. Normalized mean potential temperature profiles, as a function of z/Z_i. Curve A represents the measured values, curve B the calculated values.$_m$

.4, .5, .6, .7, .8, .9, and 1.0 Z_{i_c}. Whenever there is tower data that matches the height of one of these bins with $z \leq Z_{i_m}$ and $z \leq Z_{i_c}$, both the measured and calculated values at that level are added to their respective ensembles. Because different data periods are added into each bin, the actual shapes of the profiles have little meaning; rather it is the difference between the measured and calculated curves that is of interest. For temperature, we see that the calculated profile agrees with the measured profile to better than 10% (≈ 0.15°C) in the lowest half of the boundary layer. For $z > 0.5\ Z_{i_m}$ however, the measured profile is considerably warmer (up to 0.5°C) because of entrainment at the inversion interface. The standard deviation between calculated and measured temperatures varied from approximately 0.15°C for $z/Z_i < 0.5$ to 0.4°C for $z/Z_i > 0.5$.

For comparison to the inversion-rise model calculation of mixed-layer temperature, we also calculate θ_{BL} by taking it to be equal to the profile temperature extrapolated to $0.2\ Z_{i_c}$. Individual values and their average vs. time are shown in Figs. 20a,b. By comparing to Figs. 18a,b, we see that the surface layer profile method gives a much more accurate mixed layer temperature than the inversion rise model.

Next we consider the profile of mean wind speed. Again we assume the $\overline{U}(z)$ follows its surface layer profile up to $0.2\ Z_{i_c}$, and is constant above that. An example of calculated and measured values at the 150 m level is shown in Fig. 21a. We note the predominance of light winds, so that even at these upper levels ≈90% of the runs have $\overline{U} < 4$ m s^{-1}, with an average wind speed of ≈2.4 m s^{-1}. The ensemble $\overline{U}/u_{*_c}$ profiles are given in Fig. 21b. We see that the prediction is quite accurate, with the maximum bias at any level less than 10% of the measured wind speed. Standard deviations between calcu-

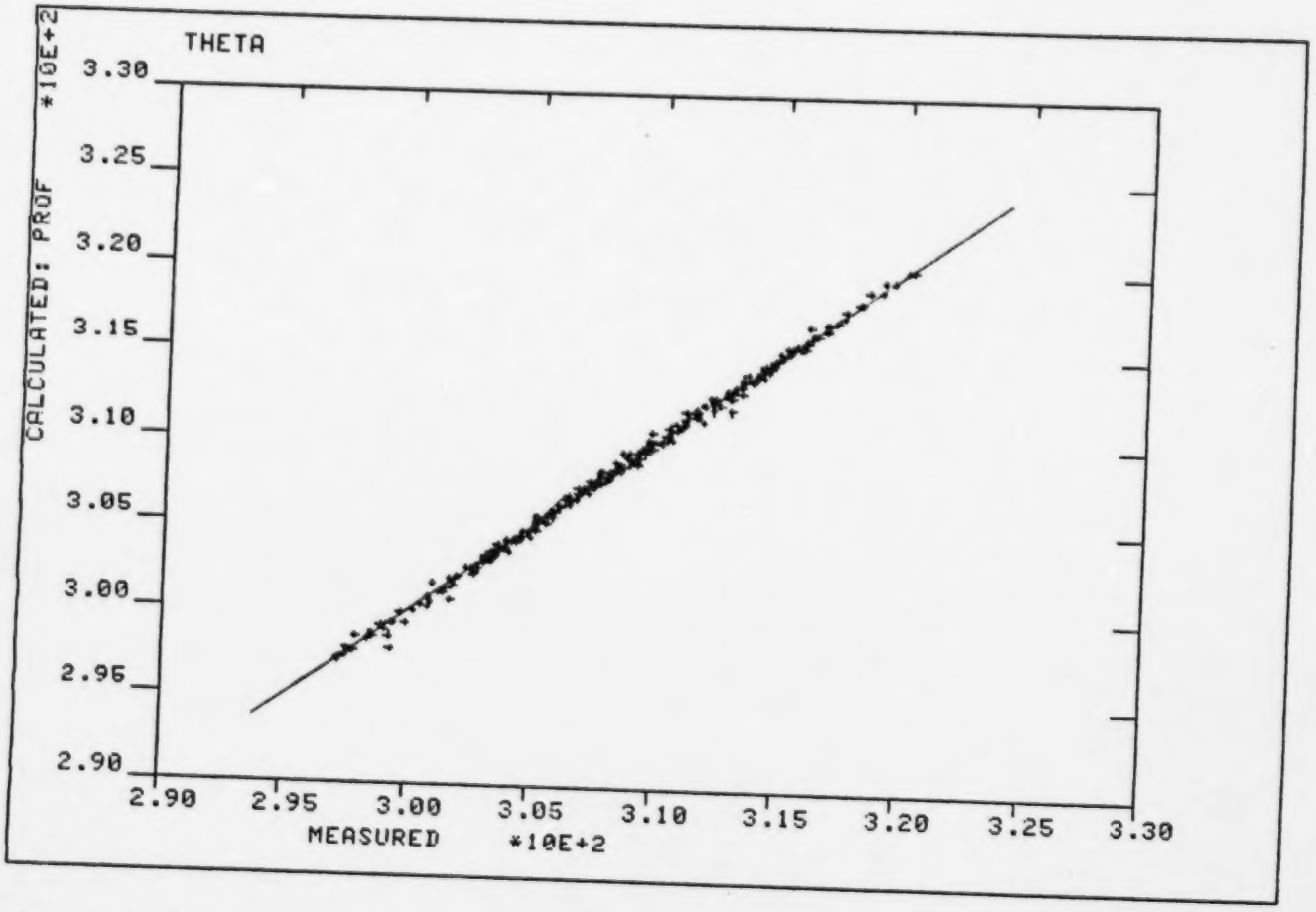

Fig. 20a. Profile derived mixed layer temperature vs. measured values.

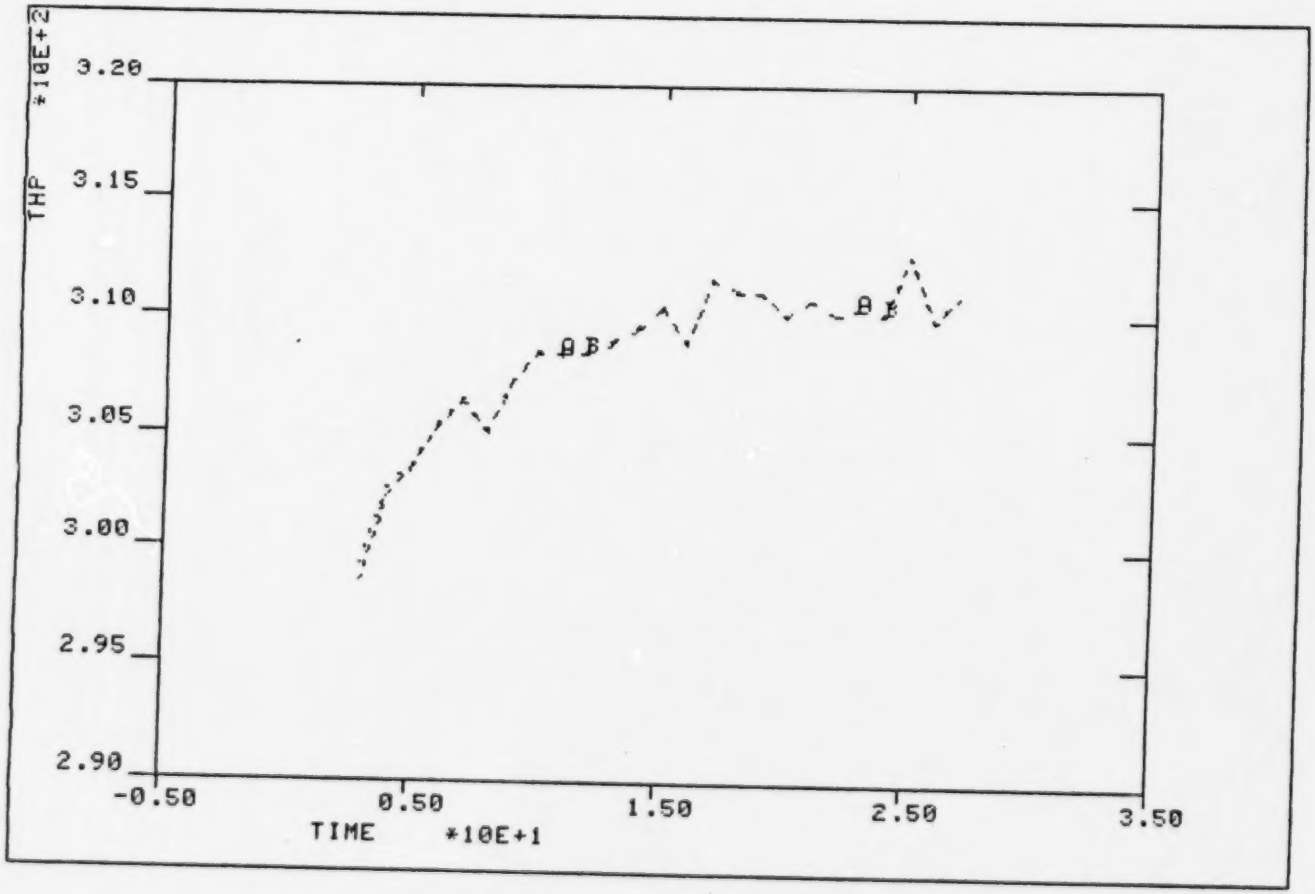

Fig. 20b. Ensemble profile derived mixed layer temperature (curve B) and measured values (curve A) as a function of time from sunrise.

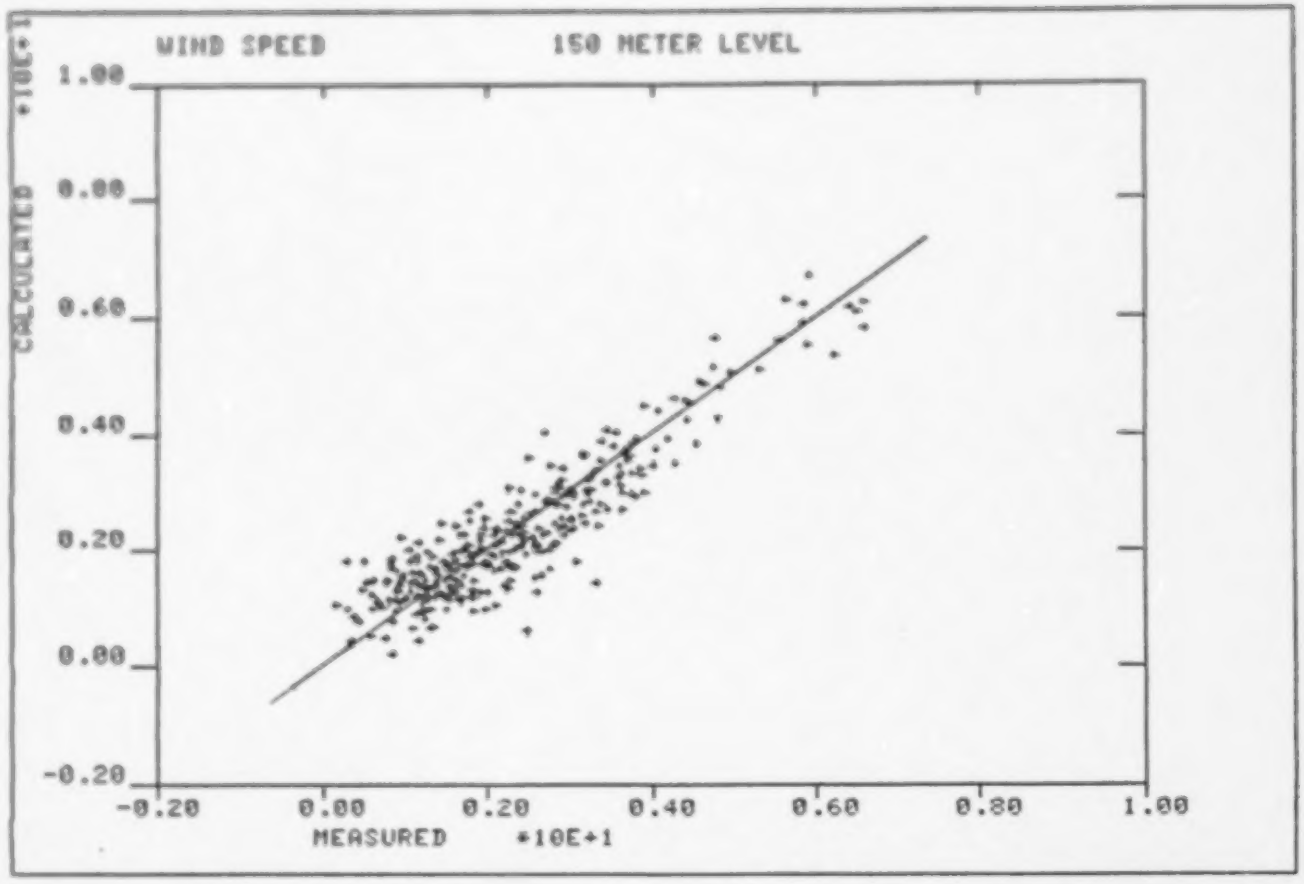

Fig. 21a. Calculated and measured windspeeds at z = 150 m.

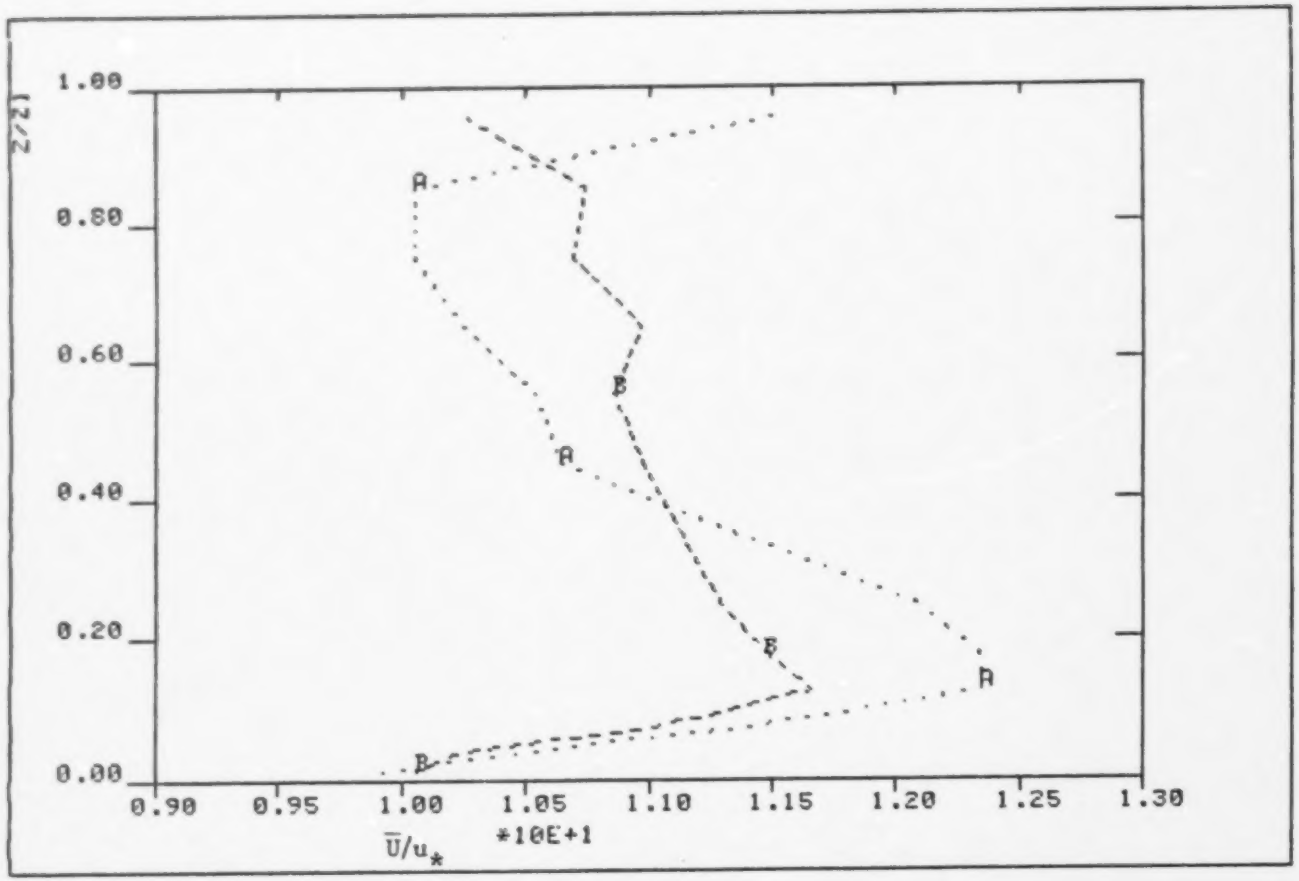

Fig. 21b. Normalized mean windspeed profiles, as a function of z/Z_{i_m}. Measured values are given by curve A, calculated by curve B.

lated and measured values were generally less than 0.6 m s^{-1} throughout the ABL.

For the wind azimuth profile we simply assume that $\overline{AZ}$ at any level in the boundary layer is the same as its surface layer value $\overline{AZ}_s$. The ensemble profile of $\overline{AZ}$ (Fig. 22a) indicates that there is in fact negligible consistent turning of the wind in the lower half of the ABL. The upper regions of the ABL do however show a clockwise turning with height, reaching approximately 20° at $z = Z_{i_m}$. At first glance this would appear to be a classic example of Ekman layer turning. However, examination of the actual wind directions reveals that the upper level winds are predominantly out of the south, rotating to a more easterly component near the surface. Since this is the same direction as that of the upslope forcing, the turning of the wind could be thermally and not frictionally induced. In fact, because the easterly upslope flow occurs on the vast majority of days, (i.e., it exists for a wide range of geostrophic wind directions), it would seem likely that the observed turning of the wind is in fact thermally forced, and not an Ekman spiral.

The mean azimuth error together with curves representing ± one standard deviation of the difference between measured and predicted values from the bias are given in Fig. 22b. The standard deviation is less than 35° in the lowest half of the boundary layer, increasing to approximately 60° in the upper ABL. Hour averages of $\overline{AZ}$ show no decrease in these large deviations, indicating that sampling errors are not their cause. Instead we again attribute these large values to the fact that no matter what the upper level (geostrophic) wind direction is, the surface wind nearly always has an easterly component.

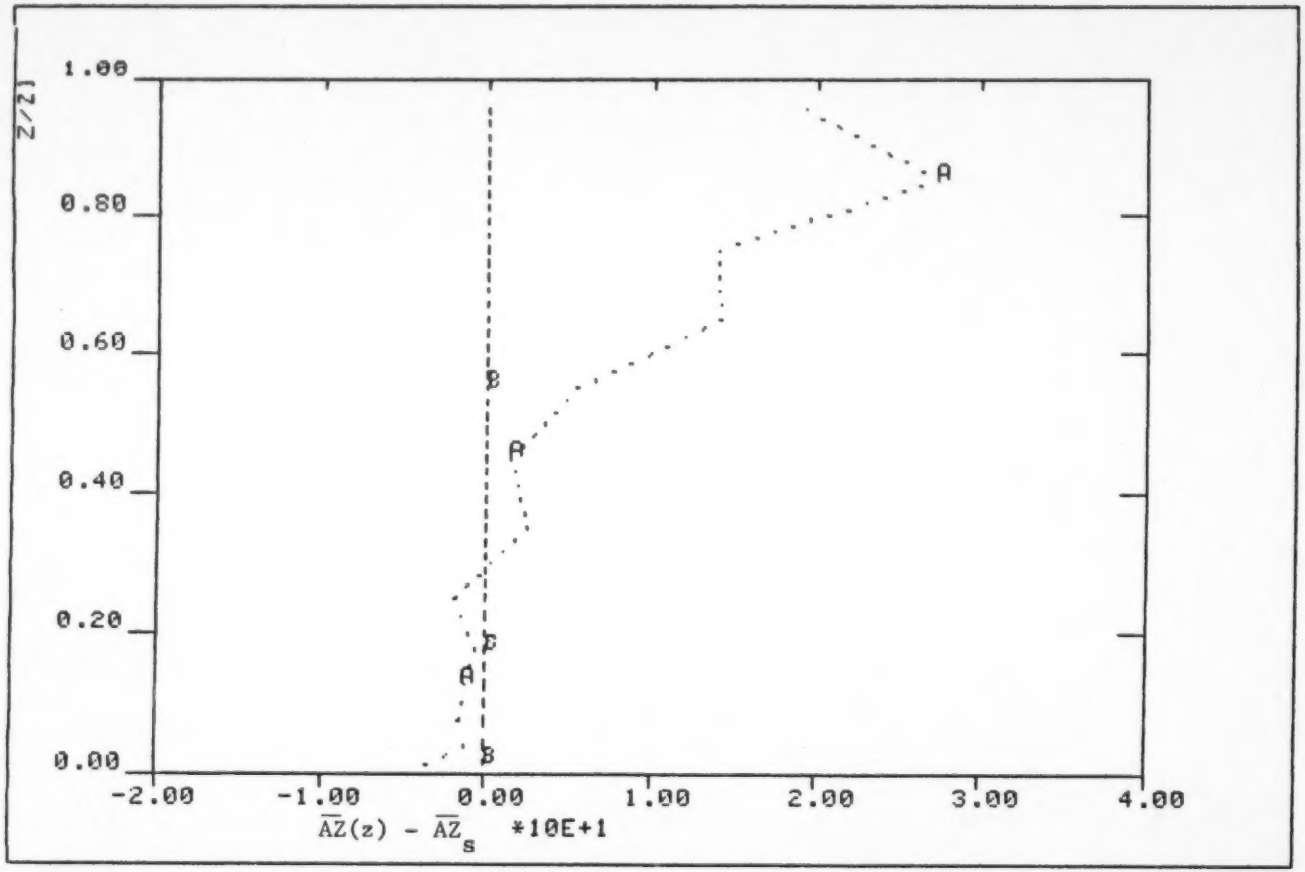

Fig. 22a. Average wind azimuth profile vs. z/Z_{i_m}. Positive values denote clockwise turning with height.

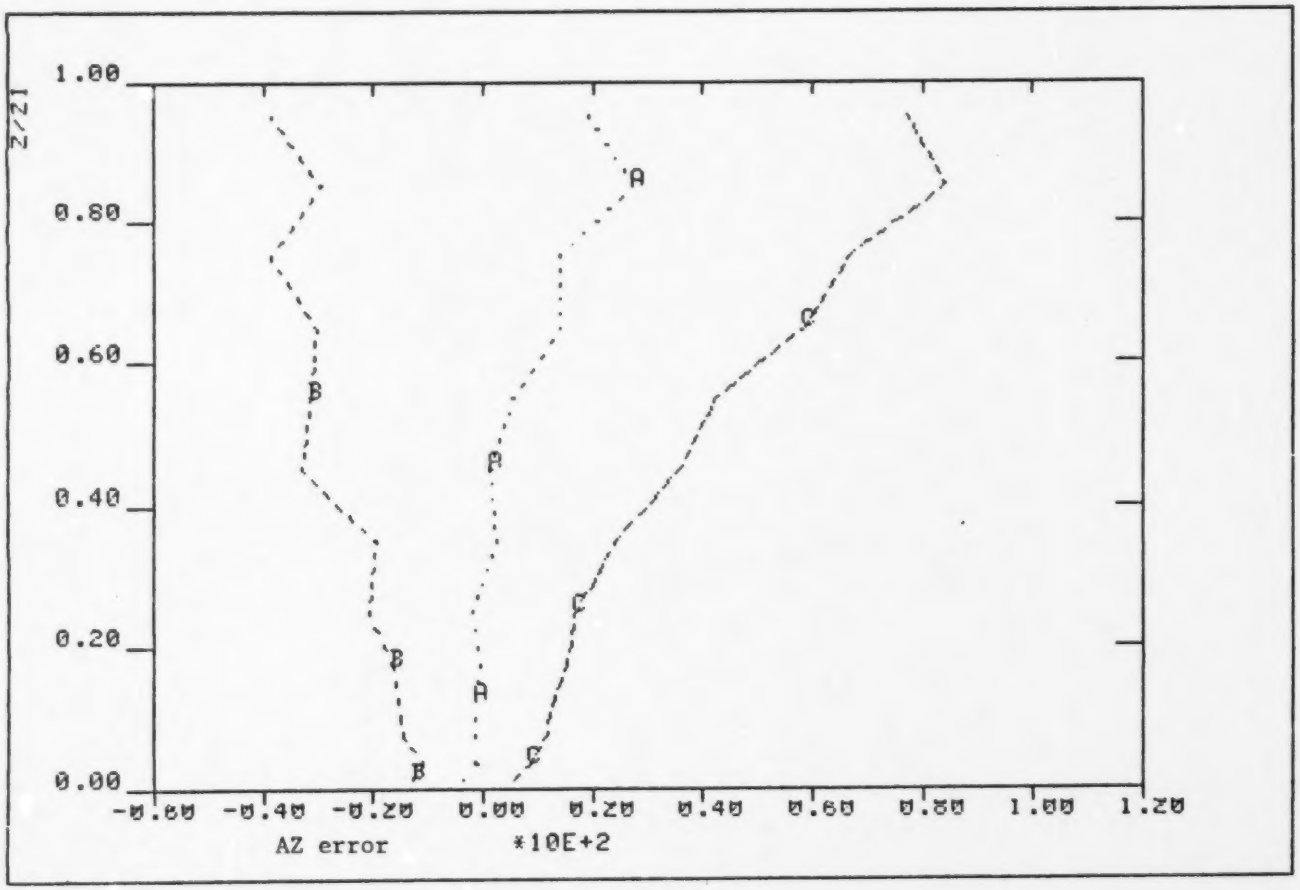

Fig. 22b. Mean bias (curve A) and error (curves B and C) of the wind azimuth prediction.

The differences between calculated and measured wind azimuths will of course be a function of wind speed, with the differences decreasing as the wind direction increases. For this reason we have also calculated the two vector components of the wind, $\vec{U}$ and $\vec{V}$, where $\vec{U}$ is in the direction of $\overline{AZ}_s$ and $\vec{V}$ is positive 90° clockwise from $\vec{U}$. We see in Fig. 23a that $\vec{U}_m$ decreases more rapidly with height than $\overline{U}_m$ did, due to the turning of the wind. The ensemble cross-stream component (Fig. 23b) is <10% of $\vec{U}_m$ in the lower ABL, increasing to ≈50% of $\vec{U}_m$ in the upper ABL.

Before computing the turbulent velocity variances throughout the predicted depth of the ABL, we first tested the variance profiles (56-57) derived in Sec. 5 against the current data set. Figure 24 demonstrates the validity of the σ_w profile, where here we have used Z_{i_m} and w_{*_m} to calculate σ_w.

In Fig. 25a we have again used (57) to calculate σ_w, but now we have used the calculated instead of the measured values of Z_i and w_*. The relatively large scatter in this figure (≈ 25%) is reduced in half when hour averages are used, again demonstrating the effect of averaging time on an individual realization. In an ensemble form (Fig. 25b), the values of σ_{w_m} and σ_{w_c} are both normalized by w_{*_c} (so they can be easily compared) and are plotted vs. z/Z_{i_m}. In the lower half of the boundary layer the two are in agreement to within 15%. The major difference between the two values is that σ_{w_m} drops off considerably faster than σ_{w_c} for $z/Z_{i_m} > 0.7$. This behavior, however, is simply an artifact of the normalization process. For $Z_{i_c} < Z_{i_m}$ σ_w is not calculated in the vicinity of Z_{i_m}, and no data goes into the ensemble averages; but when $Z_{i_c} > Z_{i_m}$, we will have $\sigma_{w_c} > \sigma_{w_m}$ near Z_{i_m}.

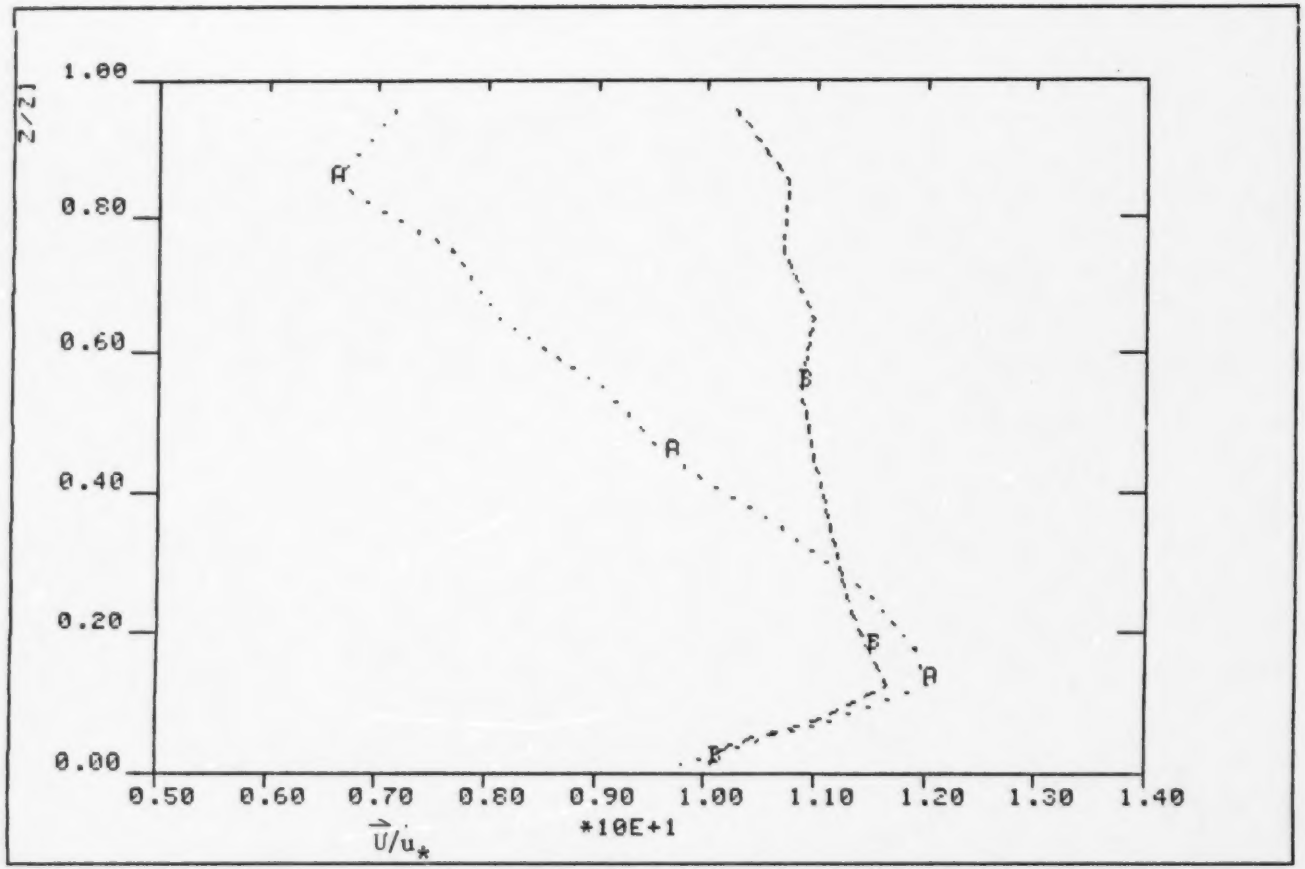

Fig. 23a. Normalized mean vector wind velocity profiles, as a function of z/Z_{i_m}. Curve A represents the measured values, curve B the calculated values.

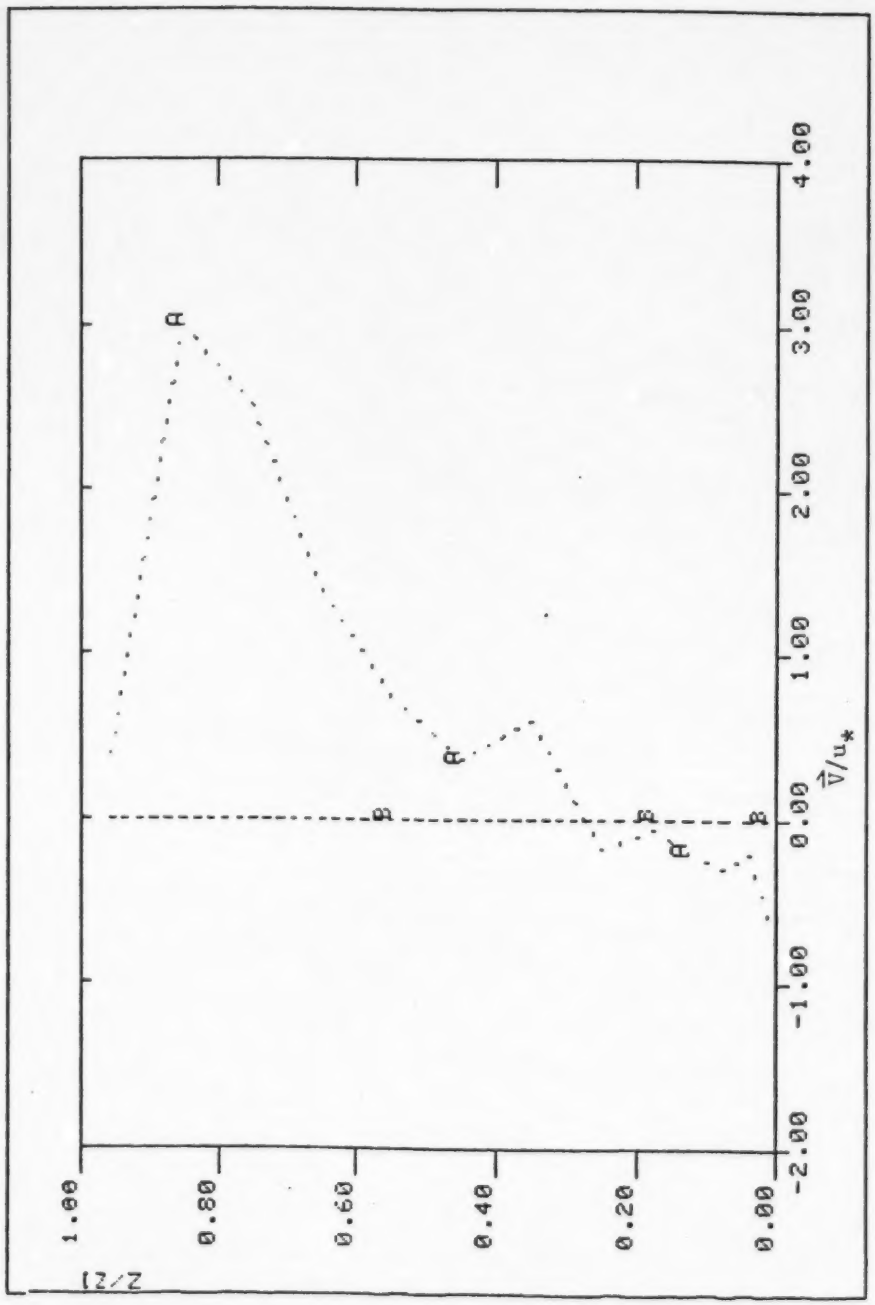

Fig. 23b. Normalized lateral wind velocity profile as a function of z/z_{i_m}.

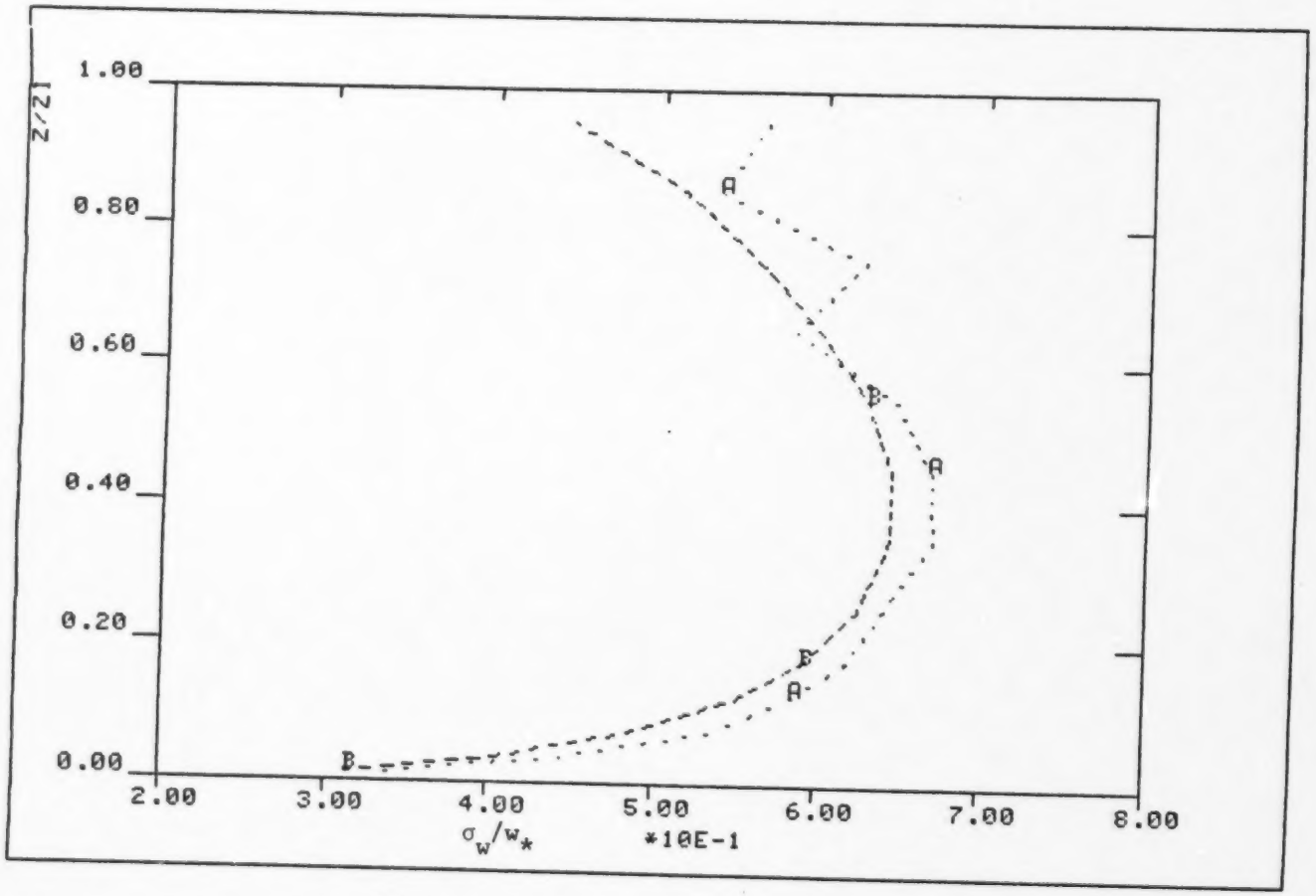

Fig. 24. Normalized σ_w profiles, as a function of z/Z_{i_m}. Curve A represents measured values, curve B calculated values derived using measured values of Z_i and $\overline{w'\theta'}_o$.

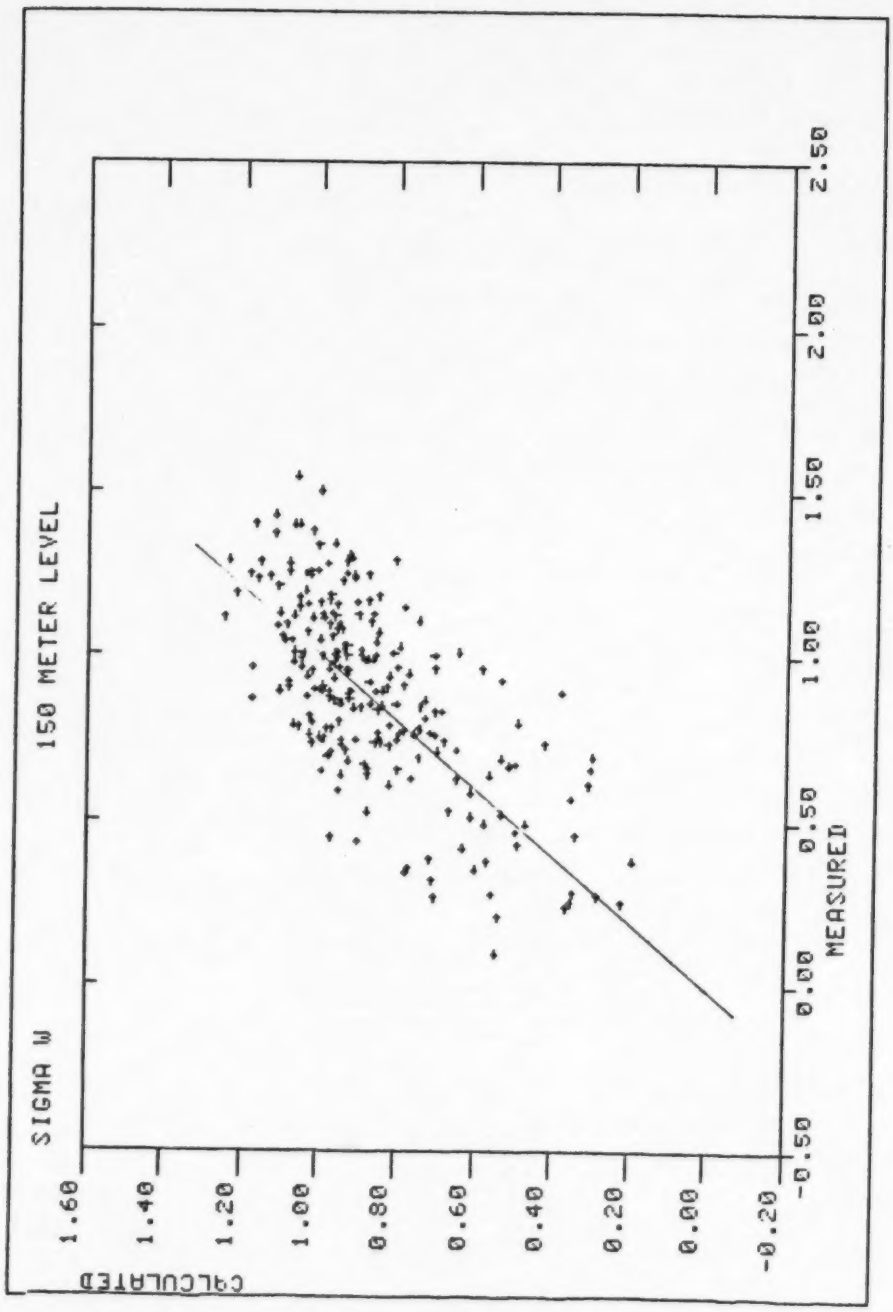

Fig. 25a. Predicted and measured values of σ_w at z = 150 m.

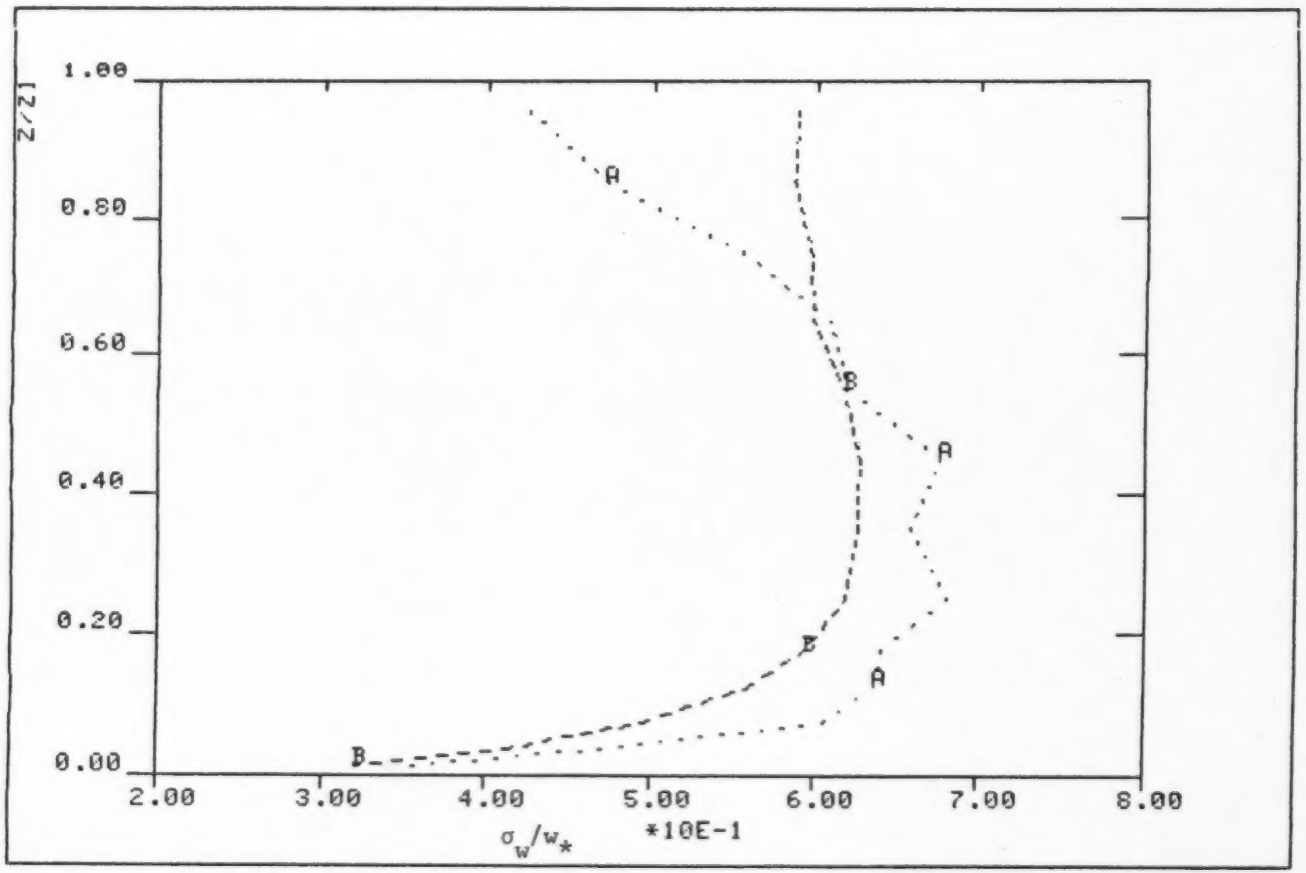

Fig. 25b. As in Fig. 24, except the calculated values are derived using predicted values of Z_i and $\overline{w'\theta'}_o$.

Because σ_{w_c} and σ_{w_m} are defined over different ranges ($0 < z < Z_{i_c}$ and $0 < z < Z_{i_m}$) this problem will always be present.

In a similar fashion we present individual values of σ_u and σ_v (Figs. 26a and 27a) as well as their ensembles (Figs. 26b, 27b). Again the standard deviation of σ_u and σ_v can be reduced considerably (from 25% to 15%) by increasing the averaging time to one hour. The ensemble σ_{u_c}/u_{*_c} profile agrees with the σ_{u_m}/u_{*_c} profile to within ≈5%, while the σ_v profiles agree to within ≈10%.

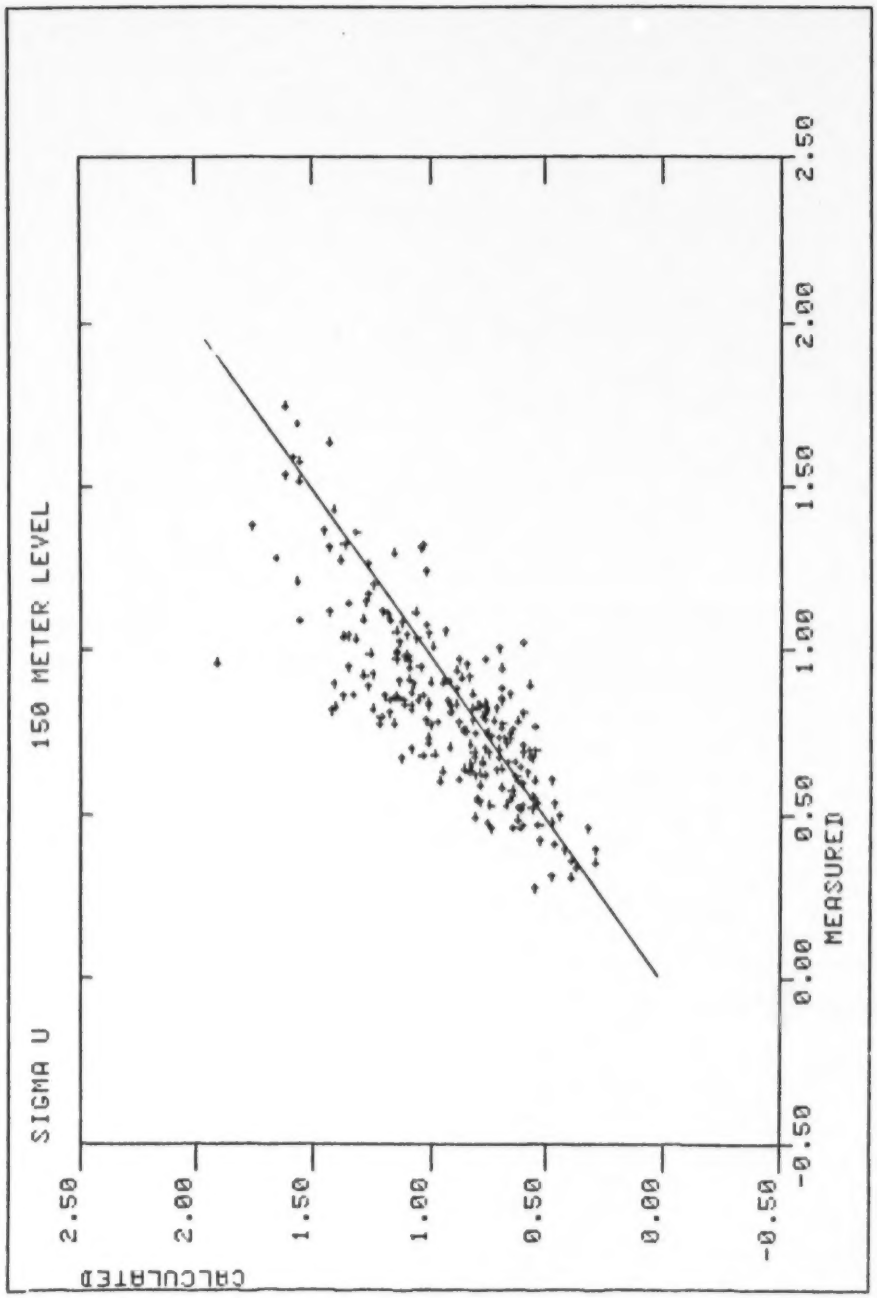

Fig. 26a. Predicted and measured values of σ_u.

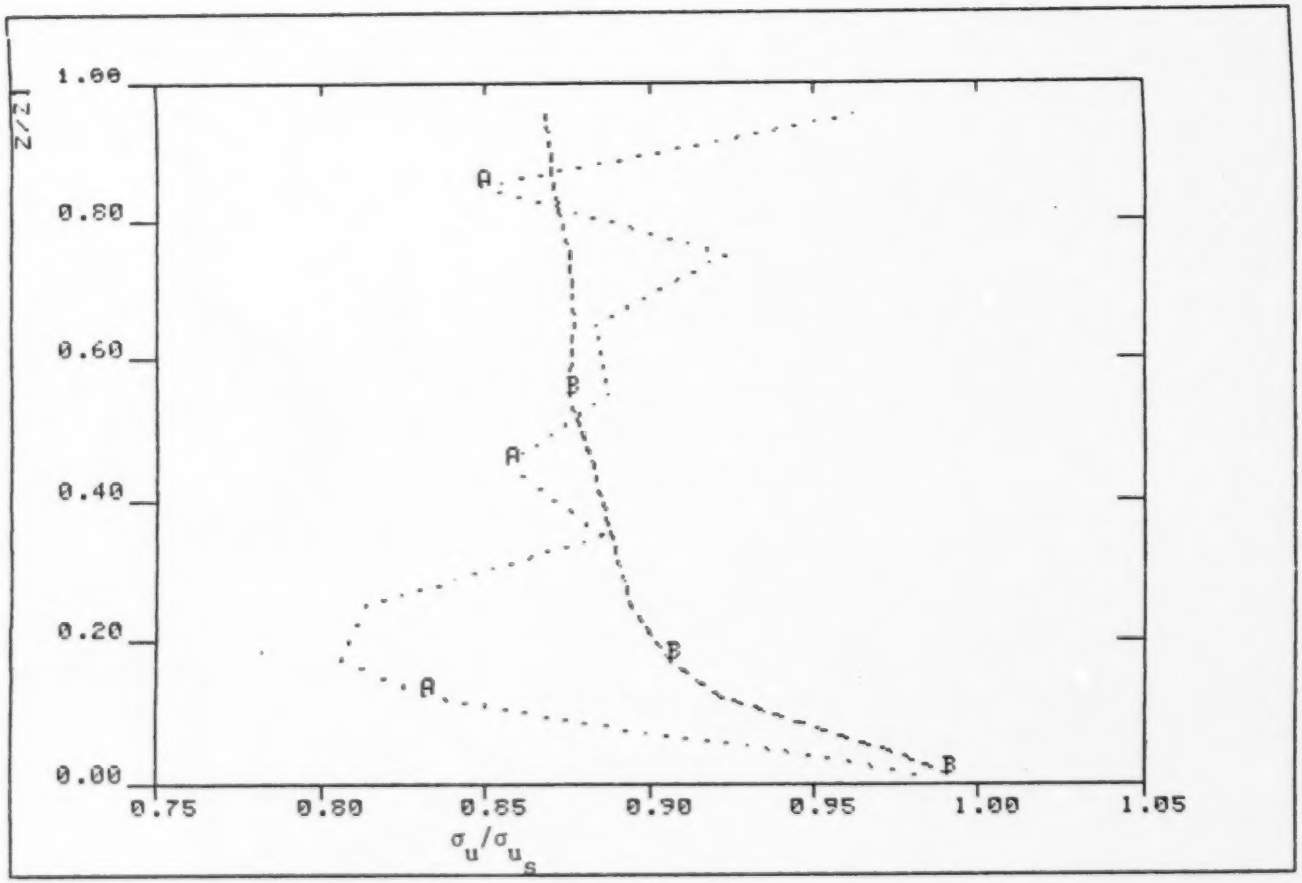

Fig. 26b. Normalized σ_u profiles, as a function of z/Z_{i_m}. Curve A represents measured values, curve B calculated values.

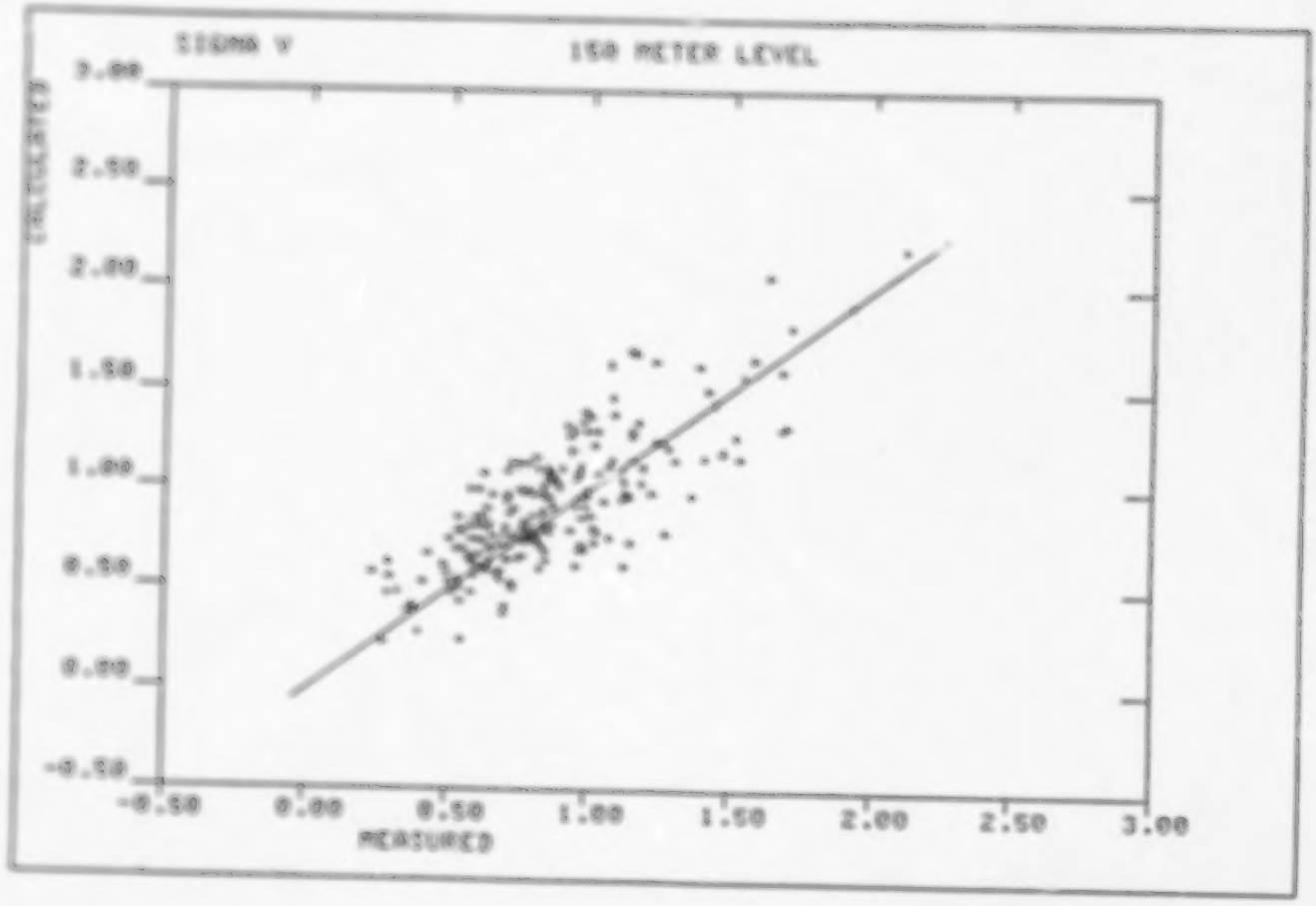

Fig. 27a. Predicted and measured values of σ_v.

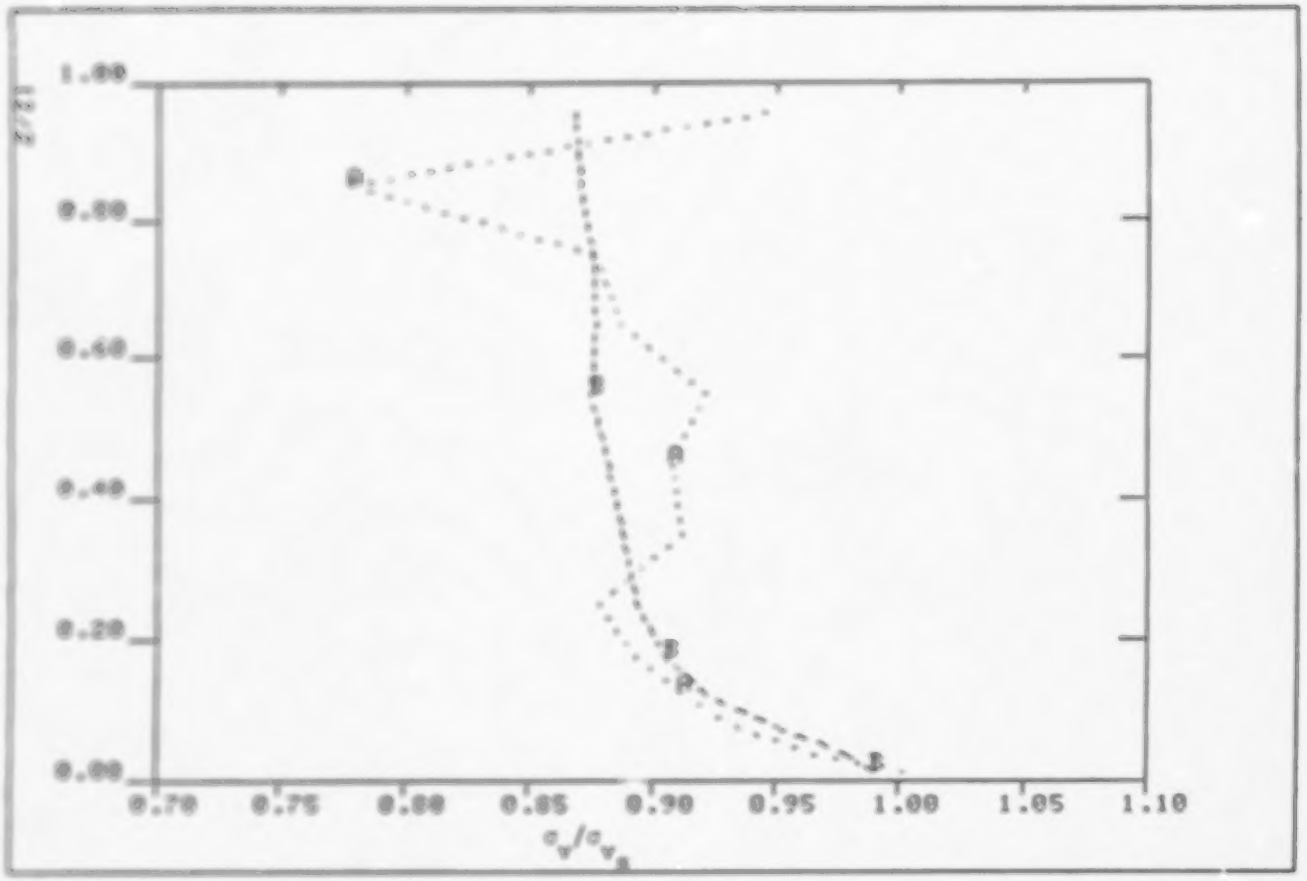

Fig. 27b. As in Fig. 26b., for σ_v.

SECTION 7

SUMMARY AND CONCLUSIONS

The purpose of this study has been to demonstrate the accuracy to which the mean and turbulent structure of the convective atmospheric boundary layer can be determined, by use of indirect estimates of the surface fluxes which are based on simple surface layer measurements. Ensemble averages of heat flux and stress indicate that these fluxes can be estimated in the mean to within about 10%. The standard deviation of the difference between calculated and measured, relative to the mean difference, is ≈50% of the mean for 20 min averages of heat flux, decreasing to ≈30% of the mean for one hour averages. Since the ensemble mean smooths out some of the differences due to non-stationarity, inhomogeneity, etc., while the hour averages still contain differences from a true spatial mean due to a limited sampling time, the actual accuracy of an individual predicted value of heat flux will most likely fall somewhere in between. For heat flux this gives $0.1 \leq \text{error } (\overline{w'\theta'}_c/\overline{w'\theta'}_m) \leq 0.3$, while for stress the error bounds increase to $0.3 \leq \text{error } (\overline{u'w'}_c/\overline{u'w'}_m) \leq 0.7$.

Using the calculated surface fluxes, inversion heights are then derived. The ensemble average inversion heights agree almost exactly with the measured values, while the standard deviation of individual realizations is about 30% of the mean. Mixed layer temperatures are much more accurately deduced (to within ≈0.2°C) by extrapolation of the surface layer $\overline{\theta}(z)$ profile than by the

mixed layer model. Advection, terrain inhomogeneities and inversion based shear combine to give θ_{BL} errors from the mixed layer model at least an order of magnitude larger than those from the profile method.

The mean potential temperature profile, $(\overline{\theta}(z) - \overline{\theta}(2))/\theta_{\star_c}$, has an associated mean bias and standard deviation of ≈ 10% in the lowest half of the ABL. This corresponds to approximately 0.15°C. In the upper half of the ABL, entrainment associated heating can lead to a bias error on the order of 0.5°C, while the standard deviation increases to 30%.

Wind speed profiles also have a mean error range of 10% to 30% in the present data set. This error corresponds to an actual wind speed error range of 0.2 m s^{-1} to 0.6 m s^{-1}.

The mean wind direction has proven to be the most difficult parameter to predict accurately. The reason for this is that even gentle slopes in the terrain (on the order of 0.01) will induce significant thermally forced circulations. In light to moderate geostrophic winds, the thermally forced flow can cause significant directional shear across the ABL depth. For strong geostrophic winds or for flat, uniform sites, we expect that the accuracy in predicting $\overline{\Delta\theta}(z)$ would increase significantly.

The errors for the turbulent velocity components $\sigma_{u,v,w}$ all have similar values with a mean bias of approximately 15% and a standard deviation of 25%. These ranges correspond to roughly 0.15 to .25 m s^{-1}.

In conclusion, we see that most of the meteorological parameters needed for routine dispersion estimates can be predicted with a mean error of

approximately 10 to 30%. The most difficult parameter to predict is the wind direction in situations of inhomogeneous terrain and light geostrophic winds.

The effect of averaging time on acquiring an accurate estimate of the true ensemble mean of a turbulent moment has been emphasized. Because averaging time increases both with the order of the turbulent moment and with height, extremely long averaging times will be required to obtain accurate directly measured values of $\sigma_{u,v}$ and σ_w through the depth of the ABL. For example, Wyngaard (1973) shows that the averaging time required to measure $\overline{w'^2}$ to a fixed accuracy increases linearly with height; this means that at 100 m one needs ten times the averaging period as at a 10 m height! For this reason one may actually attain a more representative value of the true ensemble turbulent moments by use of an indirect method, based on measurements of first order parameters such as $\overline{U}$ and $\overline{\theta}$, than by directly measuring the turbulent moments with in-situ sensors. Furthermore, unless a remote sensor provides area averaged measurements, as in a vertical azimuth display (VAD) scan, it is likely that the indirect method will still provide the most representative value of the true ensemble turbulent moment.

REFERENCES

Businger, J. A., J. C. Wyngaard, Y. Izumi and E. F. Bradley, 1971: Flux profile relationships in the atmospheric surface layer. J. Atmos. Sci., 28, 181-189.

Caughey, S. J., and S. G. Palmer, 1979: Some aspects of turbulence structure through the depth of the convective boundary layer. Quart. J. Roy. Meteor. Soc., 105, 811-827.

Driedonks, A. G. M., 1982a: Models and observations of the growth of the atmospheric boundary layer. Bound.-Layer Meteor., 23, 283-306.

Driedonks, A. G. M., 1982b: Sensitivity analysis of the equations for a convective mixed layer. Bound.-Layer Meteor., 22, 475-480.

Dyer, A. J. and E. F. Bradley, 1982: An alternative analysis of flux-gradient relationships at the 1976 ITCE. Bound.-Layer Meteor., 22, 3-19.

Korrel, A., H. A. Panofsky and R. J. Rossi, 1982: Wind profiles at the Boulder tower. Bound.-Layer Meteor., 22, 295-312.

Nieuwstadt, F., 1978: The computation of the friction velocity u_* and the temperature scale T_* from temperature and wind velocity profiles by least-square methods. Bound.-Layer Meteor., 14, 235-246.

Schotz, S., and H. A. Panofsky, 1980: Wind characteristics at the Boulder Atmospheric Observatory. Bound.-Layer Meteor., 19, 155-164.

Swokowski, E. W., 1979: Calculus with Analytic Geometry. Prindle, Weber and Schmidt, Boston MA. Pgs. 539-542.

Tennekes, H., 1973: A model for the dynamics of the inversion above a convective boundary layer. J. Atmos. Sci., 30, 558-566.

Willis, G. E., and J. W. Deardorff, 1974: A laboratory model of the unstable planetary boundary layer. J. Atmos. Sci., 31, 1297-1307.